An Integrated Three-Dimensional Aeromechanical Analysis for the Prediction of Stresses on Lift Offset Coaxial Rotors

Mrinalgouda Patil[1], Ravi Lumba[2], Buvana Jayaraman[3] and Anubhav Datta[4]

[1] Postdoctoral Associate, Aerospace Engineering, University of Maryland, College Park, USA
[2] Science and Technology Corp, Ames Research Center, Moffett Field, CA, USA
[3] U.S. Army Combat Capabilities Development Command, Aviation and Missile Center, Moffett Field, CA, USA
[4] Associate Professor, Aerospace Engineering, University of Maryland, College Park, USA

ABSTRACT

This paper presents the first application of an Integrated Three-Dimensional aeromechanical analysis—defined as the coupling of three-dimensional finite element-based structural dynamics with a three-dimensional Reynolds-Averaged Navier-Stokes-based fluid dynamics—to predict the stresses on a lift-offset coaxial rotor. The coupling was carried out with the University of Maryland structural dynamic solver X3D and the U.S. Army CREATE™–AV Helios suite of fluid dynamic solvers. A modern four-bladed hingeless coaxial rotor model—inspired by the gross dimensions of the Sikorsky S-97 Raider but generic and open source otherwise—is developed as a demonstration test case. The new structural analysis is both enabled and driven by advanced high-performance computing, parallel and scalable solvers, high-order three-dimensional brick finite elements unified with multibody dynamics, integrated aeromechanics, and a special 3D-to-1D fluid-structure interface that refines the power of the delta-coupling procedure while retaining the advantages of existing CFD mesh motion schemes. The analysis predicts the three-dimensional stresses on the rotor blades and hub, together with the deformations, airloads, and wake, in an integrated manner. Three flight conditions are studied: a low-speed flight at $\mu = 0.1$, a high-speed flight at $\mu = 0.35$, and a very high-speed flight at $\mu = 0.5$. Interesting three-dimensional unsteady stress patterns are revealed all across the blade but particularly inboard of $50\%R$—patterns that change from flight to flight, with and without lift offset, and have remained invisible until now—since they could neither be predicted nor measured in flight. The key conclusion is that such analysis is now indeed possible, and the stress patterns they reveal provide deeper insights into the dynamics of advanced rotors, and these might provide a path toward mitigating them in the future.

NOTATION

a	speed of sound, ft/s (m/s)
C_p	pressure coefficient, $(p - p_\infty) \div \frac{1}{2}\rho U^2$
C_Q	rotor torque coefficient, torque $Q \div \rho ARV_t^2$
C_T	thrust coefficient, thrust $T \div \rho AV_t^2$
M	hub moment
$M^2 c_n$	sectional normal force normalized by $\frac{1}{2}\rho a^2 c$
N_b	number of blades
p	surface pressure, Pa
p_∞	free stream pressure, Pa
R	rotor radius, ft (m)
T	thrust, hub vertical force
U	section speed, $\Omega r + V \cos\alpha \sin\psi$
V_t	tip speed, ΩR
z	rotor separation distance, ft (m)
α	shaft tilt angle (positive into flow), $^\circ$
β_p	pre-cone, $^\circ$
θ_{75}	collective, $^\circ$
θ_{1c}	lateral cyclic, $^\circ$
θ_{1s}	longitudinal cyclic, $^\circ$
μ	advance ratio, aircraft speed $\div(\Omega R)$
ρ	air density, kg/m^3
σ	rotor solidity
σ_{11}	axial stress, N/m^2
σ_{12}	in-plane shear stress, N/m^2
σ_{13}	transverse shear stress, N/m^2
ψ	blade azimuth angle, $^\circ$
Ω	rotor rotation speed, rad/s

Superscripts

CCW	counter clockwise
CW	clockwise
L	lower rotor
U	upper rotor

Presented at the 49th European Rotorcraft Forum, Bückeburg, Germany, Sep 5–7, 2023.

INTRODUCTION

This paper introduces Integrated Three-Dimensional (I3D) aeromechanical analysis to study modern lift offset coaxial rotors. It is defined as the coupling of 3-D solid finite element-based computational structural dynamics (CSD) with 3-D Reynolds Averaged Navier-Stokes-based computational fluid dynamics (CFD). The structural model is a departure from the current state-of-the-art comprehensive codes, where one-dimensional (1-D) beam-based models are used for the rotor.

The University of Maryland/U.S. Army software – X3D (Ref. 1) is the solver through which 3-D CSD is introduced. The U.S. Army HPCMP CREATE™–AV Helios (Ref. 2) is the framework through which 3-D CFD is introduced. A modern four-bladed hingeless coaxial rotor model is developed as a demonstration test case. The gross dimensions are loosely based on the Sikorsky S-97 Raider rotor (Figure 1). The blade and hub internal structures are generic and open source, but realistic, and representative of a modern rotor. Only the isolated rotor system is modeled, not the entire airframe.

Figure 1: The S-97 Raider.

Objective

Achieving high speeds without compromising hover has been an enduring quest for rotary-wing aircraft. In forward flight, an edgewise single main rotor begins to run out of lift in trying to achieve roll moment balance at the hub. As the lifting capability depletes on the retreating blade—due to lower dynamic pressure, the advancing blade is forced to limit its lift to achieve roll moment balance. A hingeless coaxial allows the advancing blades to continue providing lift and uses the opposite turning rotors to cancel the moments appearing at the individual hubs. The rotor no longer runs out of lift, but the price paid is the high roll moments at the individual hubs. These must be absorbed either by more structure or by greater blade flapping to relieve the stresses.

The individual hub roll moments are quantified by a non-dimensional parameter called the lift-offset LO. It represents the lateral offset of the net lift as a fraction of the radius and is defined as:

$$LO = \frac{M^U + M^L}{T^U + T^L} \cdot \frac{1}{R} \quad (1)$$

where M are the magnitudes of the individual hub roll moments of the upper and lower rotors, denoted respectively by the U and L superscripts, T are the corresponding thrusts, and R is the rotor radius. A sketch is shown in Figure 2. The moments are added because that gives the net moment carried by the shaft connecting the two rotors even though they cancel below before reaching the aircraft. When $LO = 0$, the lift is at the hub, and the shaft carries no moment. An articulated hub could also allow its advancing blades to lift freely and absorb the moments naturally with a flap hinge. This is the classic Kamov-like solution. The penalty would be high blade flapping which at high speeds would make blade strike inevitable unless the inter-rotor vertical separation is large. Thus, the fundamental trade-off in a coaxial design is high loads versus blade strike. Lift-offset coaxial helicopters absorb high loads with stiff hingeless hubs instead of blade flapping. This prevents blade strike with minimum inter-rotor spacing consistent with the need for a low-drag hub for high-speed flight. However, absorbing high loads within allowable stresses requires a heavy hub, which impacts the entire aircraft from the hub down. To maximize the full potential of the lift-offset coaxial, hub stresses must be accurately predicted, better understood, and ultimately mitigated with minimum weight. These are the overall objectives of this research.

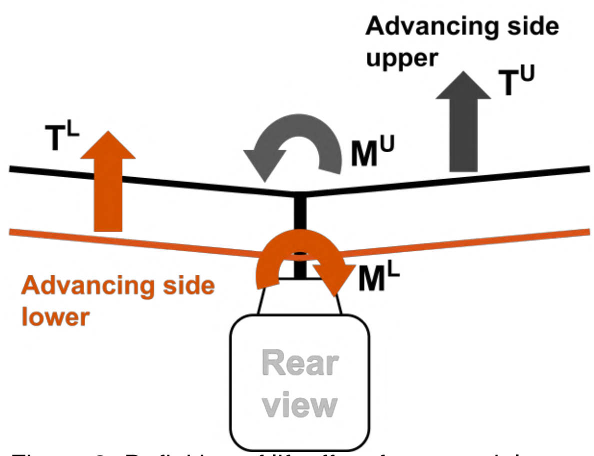

Figure 2: Definition of lift offset for a coaxial rotor.

Background

There is a vast literature on coaxial helicopters that need not be revisited here. A brief summary of the lift offset concept should suffice. The lift-offset concept was first introduced by the Sikorsky XH-59A demonstrator aircraft during the 1970s (Ref. 3). The technology was significantly advanced in the 2000s by the X2-Technology Demonstrator (Refs. 4–7), which ultimately led to the development of the larger S-97 Raider and SB>1 aircraft. These aircraft represent the cutting-edge high-speed helicopter technology together with the modern tilt rotor and the Airbus compound.

There has been a significant amount of research on lift offset coaxial rotors. They were driven by Sikorsky naturally (Refs. 8, 9), supported U.S. Government design studies (Refs. 10, 11) and small-scale hover tests (Refs. 12, 13), and academic Mach-scale hover and wind-tunnel tests at the University of Texas at Austin (Refs. 14, 15) and the University of Maryland (Ref. 16).

The most advanced of these tools have used modern CFD to resolve the coaxial flow field. But only a few studies have coupled CFD with CSD: Singh et al. for isolated model rotors (Ref. 17), Passe et al. for X2-like rotor and fuselage (Ref. 18), Klimchenko and Baeder for X2-like full aircraft (Refs. 19, 20), and Zhao et al for the S-97 full aircraft (Refs. 21, 22). All of these works have used beam-based models for structural dynamics. It is difficult to predict 3-D stresses with these models and difficult to harness the full power of 3-D CFD without resolving the detailed stresses.

Johnson and Datta (Ref. 23) identified a set of requirements for next-generation rotorcraft analysis more than a decade ago in 2008. It was envisioned to be driven by a single CAD populating both sides of the analysis—fluids and structures—with equal fidelity. Three-dimensional structural models are envisioned that would provide equal fidelity at par with three-dimensional aerodynamic models. The development of 3-D geometry and meshing tools and parallel and scalable solvers have since brought that vision to reality. The I3D coupling was born when the new software X3D demonstrated a tiltrotor test case—the NASA TRAM, a 1/4-scale model of the V-22—coupled with Helios CFD in 2018 (Ref. 24). The coaxial rotor is larger problem—it has two rotors and more than twice the number of blades—and had to wait until the time massively parallel and scalable solvers for structural dynamics could be matured. These solvers are ready now (Refs. 1, 25, 26).

However, there was no model of a full-scale coaxial rotor available for research. A model was desired that was representative of a full-scale rotor but at the same time be open-source, allow peer review, and joint investigation by the U.S. Government, industry, and academia researchers. The model in this paper was designed with these requirements in mind. The model developed in this paper, curiously named Metaltail-II (second version of a model that originally stemmed from a VFS-Army sponsored graduate design competition entry called Metailtail) is inspired by the Sikorsky S-97, but neither the geometry nor the properties bear any resemblance to the actual aircraft beyond what is already available in public domain. It is intended ultimately to be a test case for inclusion in the U.S. Army/DOD rotorcraft simulation software CREATE^{TM}–AV Helios and complement the tiltrotor model covering the two major high-speed configurations of future vertical lift.

Organization of Paper

Following this introduction, the paper begins with a description of the test case. The next two sections describe the 3-D aeroelastic solver and the structural model, followed by two sections on the 3-D CFD solver and the aerodynamic model. A brief section on X3D validation is provided followed by the I3D coupling methodology. With the description of the theory complete, the following three sections describe the results of the analysis of the three forward flight speeds. The blade pressures, airloads, deformations, and 3-D stresses are studied to understand the nature of the loading. Finally, some key conclusions are drawn.

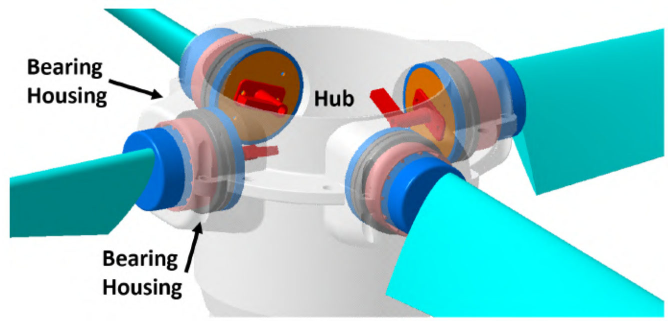

Figure 3: CATIA model of the upper rotor.

THE TEST CASE

The test case—Metaltail-II—is a notional coaxial rotor (Ref. 27). Table 1 lists the important rotor parameters. The model shares superficial similarities with the S-97 Raider, such as the hingeless hub, four blades per rotor, same rotor radius, similar planform, and similar inter-rotor spacing. The twist is -16 degrees linear, like the UH-60A Black Hawk. The hub is also notional but with enough complexity to be suitable for a test case. The cross section is a VR-7 airfoil with a D-spar and carbon-fiber skins to be representative of a modern rotor. It is a section that has been fabricated and tested on 5-ft diameter Mach-scale rotors at the University of Maryland Glenn Martin tunnel and validated for rotating frequencies and in-vacuum strains in X3D recently (Ref. 28). Thus, there is no uncertainty in the blade material properties.

The first step is a CAD model. Figure 3 shows the CATIA v5 model of the rotor. The diagram shows only the upper rotor for clarity depicting the attachment of the blades to the hub through the bearing housing. The blade root joins the individual parts – the blade, pitch horn, pitch link, outer cuff, inner cuff, thrust bearing, and journal bearing. The blade definition consists of the surface needed for aerodynamics and the internal structure needed for dynamics.

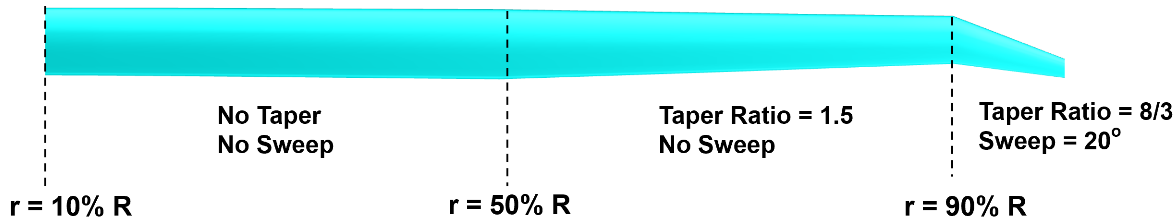

Figure 4: Blade planform depicting the taper and sweep along the span.

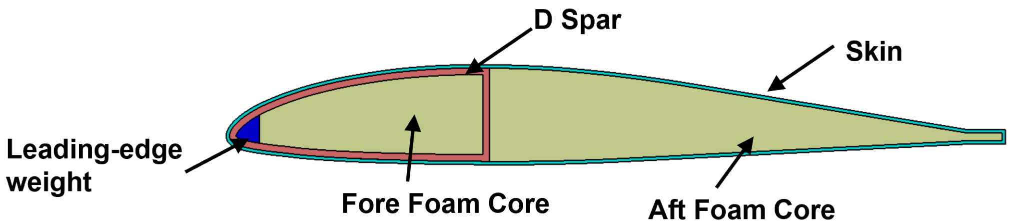

Figure 5: CAD model of the blade cross section at the root.

Table 1: Properties of the Metaltail-II rotor

Property	Value
Radius, R	17 ft (5.18 m)
Number of Blades, N_b	4
Pre-cone, β_p	1.5°
Solidity, σ	0.0636
Rotor Separation, z/D	0.07
Rotor speed, Ω	410 RPM (43 rad/s)
Mach tip, M_{TIP}	0.65

Figure 4 shows the blade planform. The span is divided into three parts: 1) from 10% R to 50% R, there is no taper or sweep; 2) from 50% R to 90% R, there is a taper ratio of 1.5 but no sweep; and 3) from 90% R to tip, there is a taper ratio of 2.66 and back sweep of 20°.

The airfoil profile is VR-7 without any tabs. The internal structure consists of a tungsten leading edge weight, a solid uni-axial carbon-fiber D-spar, a machinable foam aft core, and a uni-axial carbon fiber trailing edge block, all wrapped in a ±45° carbon fiber skin. The cross section is shown in Figure 5.

X3D SOLVER

The experimental (X) three-dimensional Dynamic (3D) Analysis for Rotors is an aeroelastic solver that can model rotor blade structures with 3-D finite elements unified with multibody dynamics (Ref. 29). Flexible parts are modeled with isoparametric 3-D hexahedral brick elements with internal nodes to allow resolving thin layers without locking. Constraints, mechanisms, and devices are modeled by joints. Joints can have mass, stiffness, and damping and can be either commanded or used as sensors. Euler angles are used for joint rotations. Transient solution is obtained using a scalable skyline solver, and the more difficult periodic trim solution is obtained using a modified harmonic balance algorithm in the complex domain built on the scalable skyline (Ref. 1). The parallel algorithms are implemented on MPI and OpenMP using a hybrid distributed-shared memory paradigm.

In addition to structural dynamics, X3D has a built-in lifting-line aerodynamic model. This model is needed as a pre-conditioner for coupling convergence. Any model that supplies aerodynamic sensitivities to deformations would suffice, for example, linear unsteady aerodynamics with uniform inflow. A full-up lifting-line model is also available which is useful for a preliminary assessment of results before launching into CFD coupling. The full-up model uses a time-accurate free wake which is also parallel but implemented only with OpenMP using a shared memory paradigm (Ref. 30). The number of processors equals the number of tip vortices. The full-up model was kept active in this work in order to concurrently assess the solution as it progressed to convergence, but it was for research purposes only, and since the results are not important for this paper, they are not shown. Most importantly, X3D has an interface to couple with CFD.

Since only the isolated rotor system is modeled, six trim controls are used: two collectives θ_{75}^U, θ_{75}^L, two longitudinal cyclics θ_{1s}^U, θ_{1s}^L, and two lateral cyclics θ_{1c}^U, θ_{1c}^L. The six trim targets are blade loading C_T/σ, zero torque $C_Q/\sigma = 0$, and individual hub roll and pitch moments which are specified on the basis of lift-offset. Alternatively, five trim controls can be used: two collectives θ_{75}^U, θ_{75}^L, two longitudinal cyclics θ_{1s}^U, θ_{1s}^L, and one lateral cyclic $\theta_{1c}^U = \theta_{1c}^L$. The five trim targets would be blade loading, zero torque, net roll and pitch moments, and a lift-offset LO. Both approaches provide similar results, but the second was easier to specify for the non-zero LO case.

The structural dynamic solution consisted of 8 harmonics and was executed on 90 processors. The lifting-line trim solution with the full-up free wake model required $2-4$ hours of wall clock time depending on the flight speed.

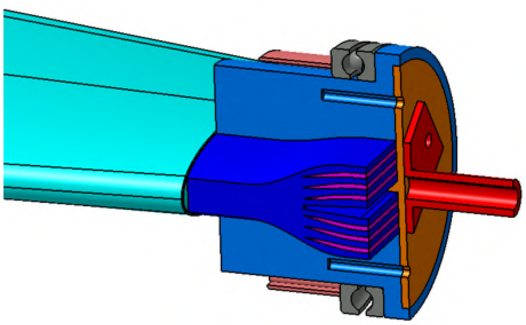

(a) Attachment of inner and outer cuff to blade

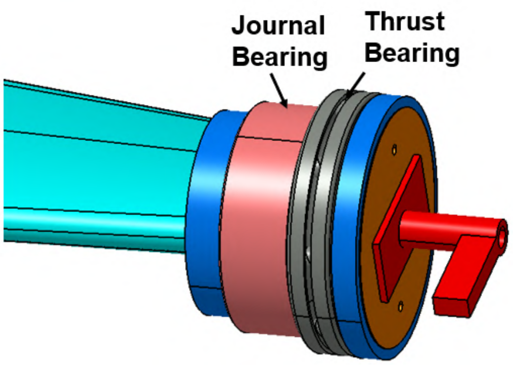

(b) Attachment of two bearings

Figure 6: Cut away view of blade root showing attachment of (a) inner and outer cuff; (b) thrust and journal bearing to the blade.

STRUCTURAL MODEL

Structural modeling begins by creating a structural analysis representation (SAR) from CAD. The SAR is not an input deck but merely an assignment on paper of the various parts and load paths to be modeled. SAR assigns parts that are to be modeled using 3-D finite elements (flexible parts with strains) and parts that are to be modeled as joints (bearings, bolts, mechanisms, and devices). There is no contact modeling. The SAR defines the type and geometry of joints, joint connections, and joint properties. The CAD drawing had five flexible parts: the blade, pitch horn, pitch link, inner cuff, and outer cuff. The bearings, fittings between the flexible parts, and hub connections are modeled as joints. Figure 3 shows how the blade root attaches to the hub. The blade root is sandwiched by the bearing housing from the top and bottom, which connects the thrust and journal bearing to the hub. The pitch horn is assembled at the root of each inner sleeve and connected to the swashplate with a pitch link.

The bolts between the inner and outer cuffs, thrust and journal bearings, and pitch link connections to the pitch horn and the hub are all modeled as joints. The exposed root of the blade mates into the inner surfaces of the outer cuff, and the inner cuff locks into the open slot of the blade as shown in Figure 6a, so the connections between the blade and both the cuffs can be modeled as rigid joints. The outer cuff is connected to the rotor hub through two bearings, as shown in Figure 6b. The thrust bearing transfers only the axial force to the hub. The journal bearing transfers thrust, in- and out-of-plane shears, and the flap and lead-lag moments. The inner cuff is connected to a pitch horn, which is then connected to a pitch link on the leading edge side of the blade. The torsion moment is transferred through the inner cuff to the pitch link, which carries it to the hub. The pitch horn and pitch link can be neglected during meshing; a root joint is sufficient for providing control inputs.

The SAR then has 9 parts, 3 of which are flexible and 6 are joints. These are shown in Figure 7 and listed in Table 2. Each part has two identifiers (ID), a part number (P#), and a type identifier (F# for flexible and J# for joint). The 3 flexible parts are meshed. The 6 joint parts are assigned kinematic constraints using Euler angles. The 3 joints that are connected to the hub also serve as load sensors for root loads. These rotating frame loads are transformed to fixed frame for hub loads. The identifier -1 sets zero displacement boundary conditions in the rotating frame. Here, it is the hub—defined as the center of rotation. Rotations commanded to the joint (P1/J1) provide pitch control for the trim solution. Figure 8 shows the load flow diagram.

The hub is assumed rigid, so the upper and lower rotors are structurally independent. A single blade is modeled in each rotor. This is sufficient for the periodic trim solution. The assumption is that the blades are identical.

Once the part types are assigned, all the flexible parts are meshed in Cubit individually with 27-node isoparametric hexahedral brick elements. The part meshes are independent, with no requirement they match at the interfaces. The meshes and joints are assembled to create the final structural analysis model (SAM) of a blade. The blades for both rotors are meshed and assembled together, as shown in Figure 9. Each rotor consists of 1920 bricks with a total of 55,000 degrees of freedom.

Each part mesh is assigned three features: blocks, sidesets, and nodesets. Blocks assign material properties, sidesets identify aerodynamic surface nodes, and nodesets act as joint connections. The meshes and joints are input to the solver through *SAM.input* file. The *SAM.input* is a FORTRAN namelist consisting of mesh positions and orientations, material properties, joint properties, and joint definitions.

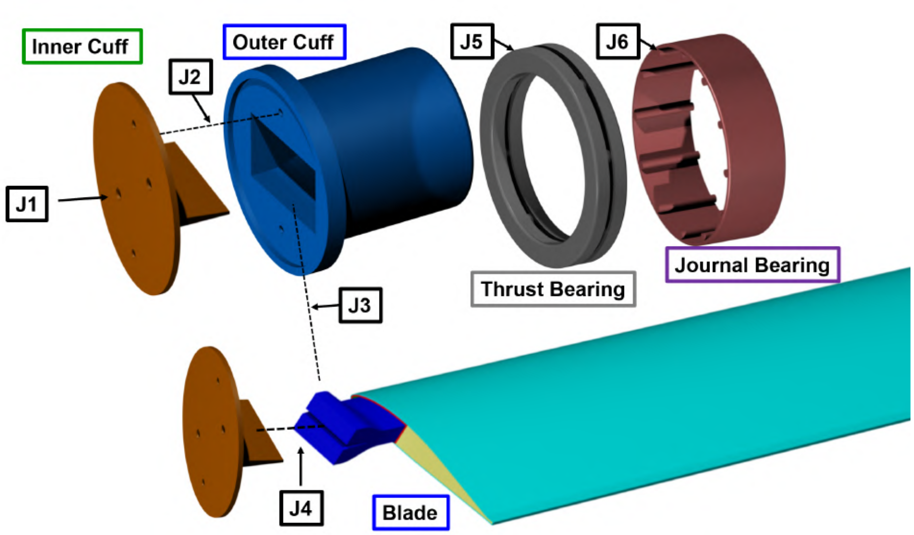

Figure 7: The 6 joints J1–J6 connecting the flexible parts.

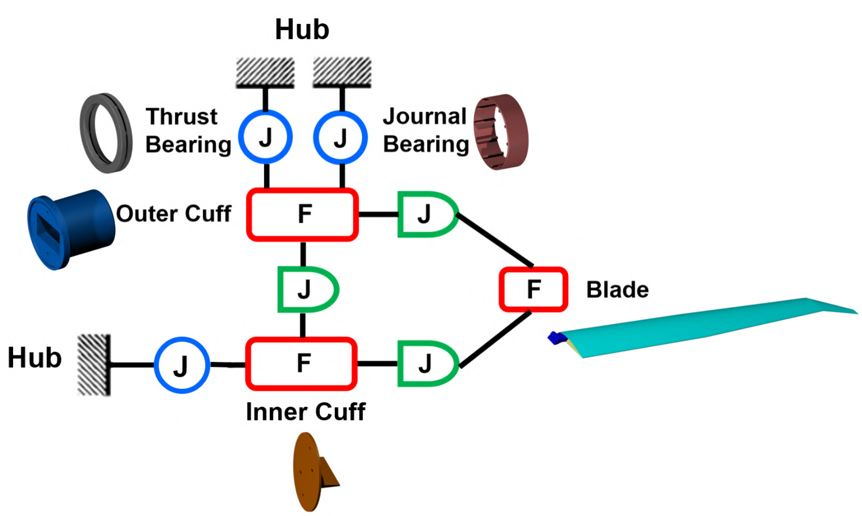

Figure 8: Load flow diagram of Metaltail-II.

Table 2: List of parts; -1 indicates boundaries.

Part No.	Flexible No. or Joint No.	Type	Connections
P1	J1	Joint	-1, P2
P2	F1	Flex	P1, P3, P7
P3	J2	Joint	P2, P4
P4	F2	Flex	P3, P6, P8, P9
P5	F3	Flex	P6, P7
P6	J3	Joint	P4, P5
P7	J4	Joint	P2, P5
P8	J5	Joint	-1, P4
P9	J6	Joint	-1, P4

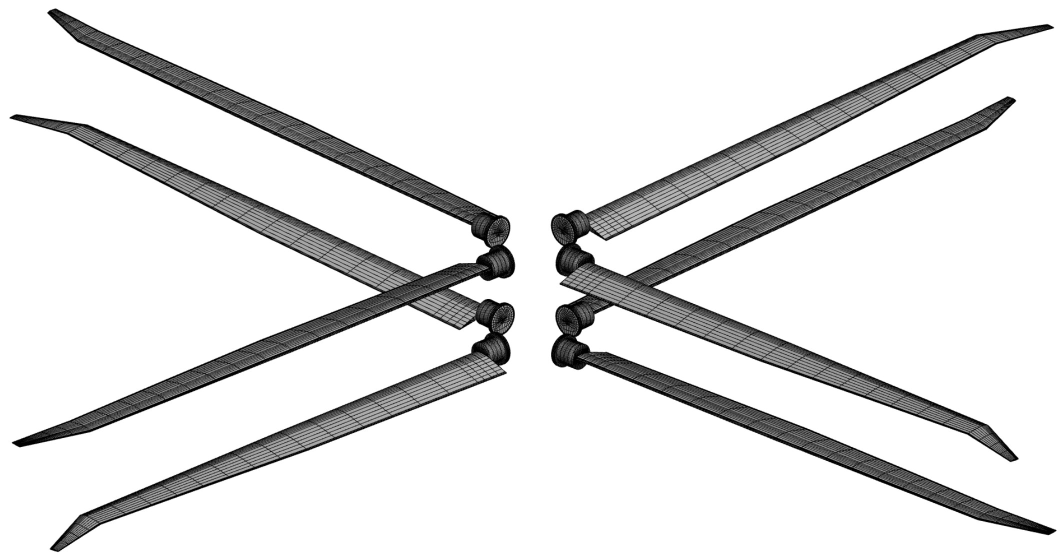

Figure 9: 3-D structural mesh of the rotor.

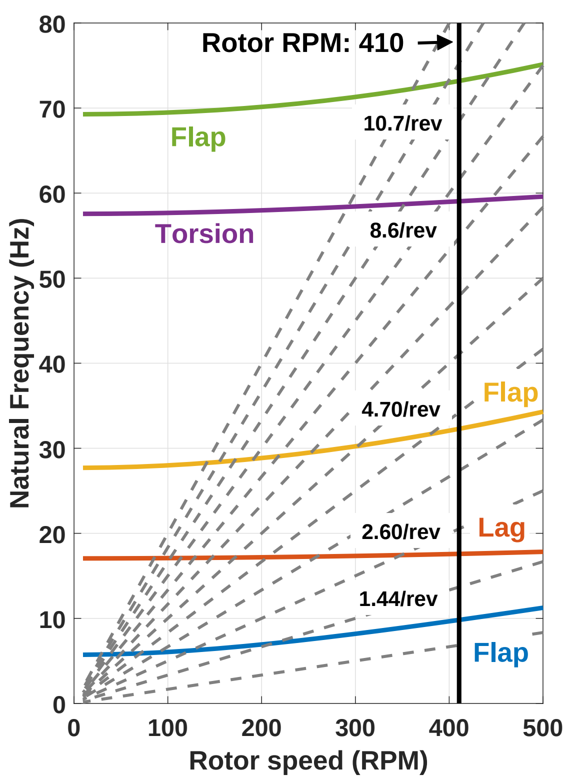

Figure 10: Rotating frequencies for the Metaltail-II rotor.

The calculated rotor frequencies are shown in Figure 10. At the nominal revolutions per minute (RPM) of 410, the frequencies clear all resonance crossings. The first flap frequency is at 1.44/rev, the first lag at 2.6/rev, and the first torsion at 8.6/rev. The first five frequencies are shown in Figure 10.

The inputs for the internal aerodynamic model consist of the lifting-line (locus of $1/4$-chord line), chord, twist, airfoil decks, and free-wake parameters. The lifting-line is swept back by 20° from $90\%\ R$. The two-dimensional C-81 airfoil decks for the VR-7 airfoil were extracted using in-house CFD. The root cut-out is $10\%\ R$. The aerodynamic model of the blade is input through a *AER.input* file. It is just another FORTRAN namelist.

HELIOS CFD SOLVER

Helios is a high-fidelity rotorcraft framework that combines state-of-the-art 3-D Unsteady Reynolds Averaged Navier-Stokes (URANS) solvers with overset capability and mesh adaptation to resolve aerodynamics loads and interactional effects (Ref. 2).

Helios uses a multi-mesh/multi-solver paradigm with the ability to use unstructured, structured, or strand meshes/solvers in the near-body region close to the solid surface to capture the viscous effects, efficient and accurate resolution of rotor wakes with a Cartesian mesh/solver with adaptive mesh refinement (SAMCart), and an implicit domain connectivity utility to automatically handle the data exchange between the different mesh systems (PUNDIT). Helios framework can integrate conventional comprehensive codes for beam-based structural dynamics comprehensive analysis codes (RCAS, CAMRADII, and X3D) to model the structural dynamics with a fluid-structure interaction utility (Melodi) to handle mesh motion and airloads integration for exchange of beam deformations and aerodynamic forces. All these components are interfaced

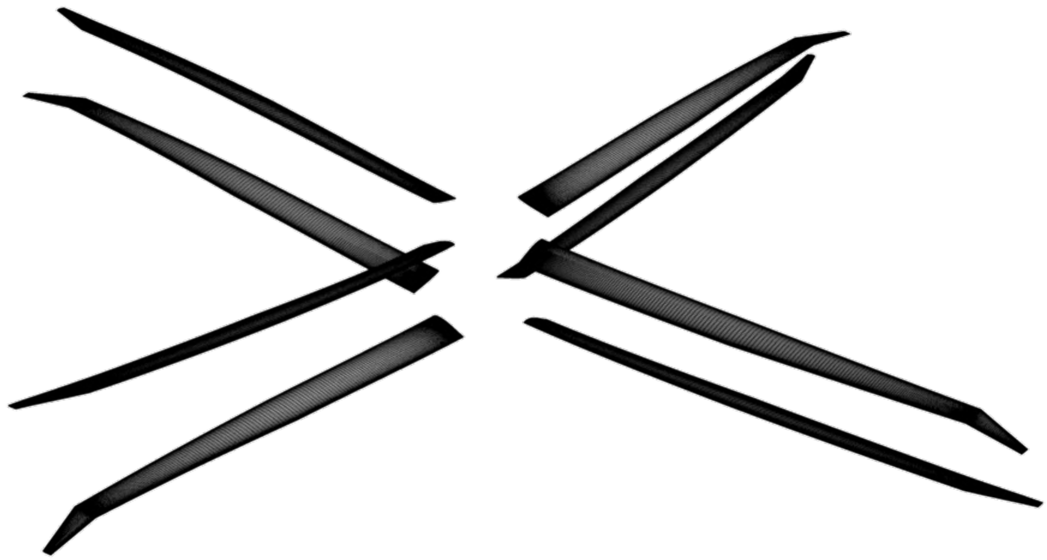

Figure 11: 3-D CFD surface mesh of the rotor.

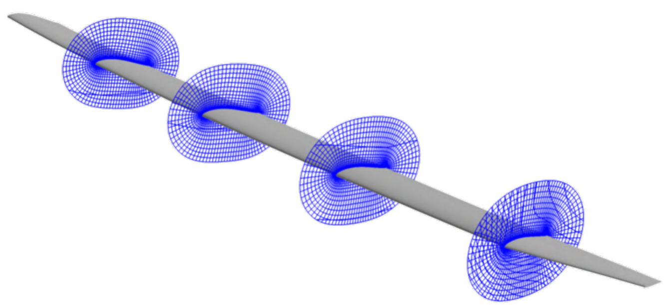

Figure 12: Near-body mesh at different spanwise sections.

together using a Python-based software infrastructure. The interface with 3-D structures is what is new in this paper.

The flow simulations were carried out using a separate set of 568 processors. Thirty sub-iterations were used in the near-body and ten sub-iterations in the off-body with a time step of 0.25 degree. Airloads and deformations were exchanged with X3D after two rotor revolutions. Each revolution takes around 11 hours of wall clock time, so the total time is 22 hours for two revolutions. Thus, the flow solver still dominates the overall solution time.

AERODYNAMIC MODEL

The aerodynamic model begins from the same CAD surface as the structure but grows outward.

Near-body Mesh

The root of the blades is simplified by excluding the complex connections to the hub and ensuring the geometry airtight. The blade surface mesh is structured and consists of 330 spanwise points and 86 chordwise points with clustering near the leading and trailing edges of the blades. Each blade mesh contains 2.4M nodes. The final assembled CFD surface mesh can be seen in Fig. 11. The near-body blade mesh extends to about one chord from the surface (Figure 12). The structured solver OVERFLOW (Ref. 31) is used as the near-body solver with the Spalart Allmaras Delayed Detached Eddy Simulation (SA-DDES) turbulence model.

Off-body mesh

The near-body meshes are placed within a set of off-body Cartesian meshes refined in 9 levels. The overall CFD domain is shown in Figure 13. It is difficult to identify all 9 levels from the figure as the overall domain extends up to 15 radii in each direction. Hence, only part of the exterior level is shown in Figure 13 to highlight the coaxial rotor. The finest spacing is 12% of the tip chord. The cells become larger away from the rotor. The far body meshes consist of a total of 450 million nodes. SAMCart is used as the off-body solver with the same SA-DDES turbulence model as the near-body solver.

X3D VALIDATION

In absence of full-scale data, the analysis was validated and verified piece-wise, as much as possible, with data from various sources. The structural model was validated with vacuum chamber data from a University of Maryland Mach-scale rotor of identical cross-section and hingeless boundary condition. The lower-order coaxial aerodynamic model was validated with

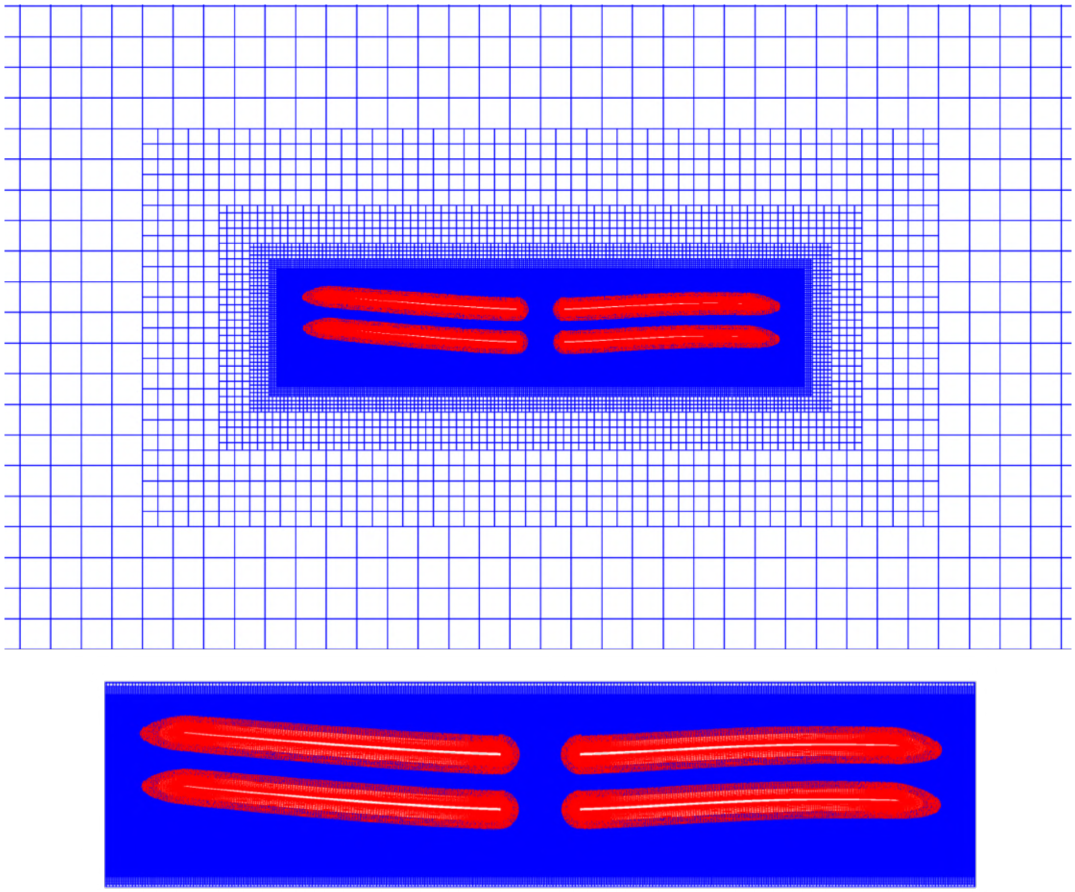

Figure 13: Full CFD domain for coaxial simulations.

hover data from U.S. Army small-scale rotor. The forward flight simulation was verified with Sikorsky published predictions, shown later in the section on LOW SPEED.

The 3-D structural model of X3D was validated with measured rotating frequencies in vacuum of a blade with a cross section identical to that of the Metaltail-II rotor (Ref. 28). The blade is straight (no taper), twisted (-16 degrees linear), with a dihedral-anhedral tip. Three identical blades were tested in a vacuum chamber (3.05-m-diam, 0.91-m-high) to measure rotating natural frequencies and strains. The rotor fan plot is shown in Figure 14. The triangles are measured frequencies; the different colors correspond to different blades. The solid lines are the predictions from X3D. Up to seven nonrotating frequencies and six rotating frequencies were captured. The corresponding modes were analyzed in X3D and are identified in Figure 14. The predictions match well with the test data except for the highest mode. The crossover of the first two modes is also observed.

The lifting-line aerodynamic model of X3D is validated with coaxial hover performance data from the U.S. Army model test (Ref. 13). The coaxial model used here is a rigid rotor with each rotor consisting of 3 blades. The blades are untwisted and rectangular with NACA 0012 airfoil. The tip Mach number is 0.25. The tip Reynolds number $(325,000)$ was low enough that Reynolds number corrections are needed. The near wake is prescribed and the far wake is free, consisting of a rolled up single tip vortex from each blade. Figure 15 shows the predictions and measurement of thrust coefficients for $C_T = 0.007$ and 0.014 versus the rotor separation distance. Regardless of the total thrust, with increasing separation, the lower rotor produces a lower thrust until the wake of the upper rotor is fully developed. Thereafter the thrust sharing is constant -— around 55% for the upper and 45% for the lower rotor. As the rotors get closer, the upper rotor thrust decreases due to the influence of the lower rotor. Overall, the analysis shows good agreement with the test data.

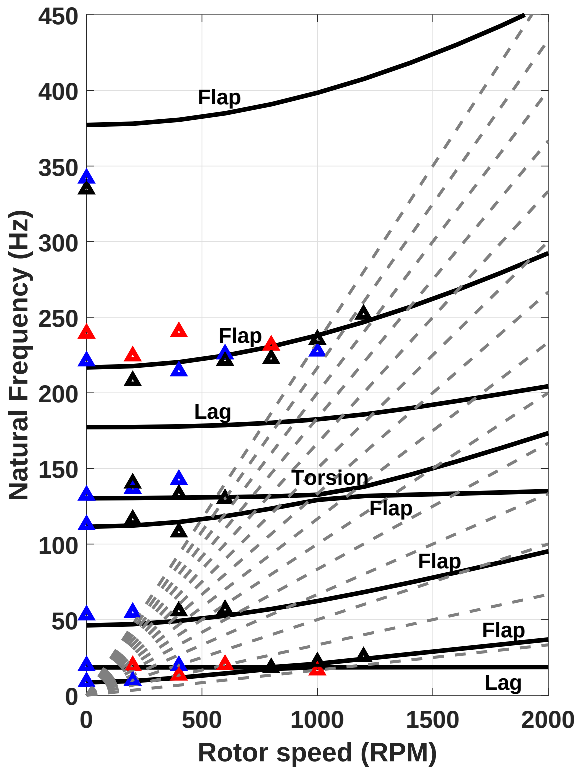

Figure 14: Measured versus predicted rotor fan plot for a blade with Metaltail-II cross section.

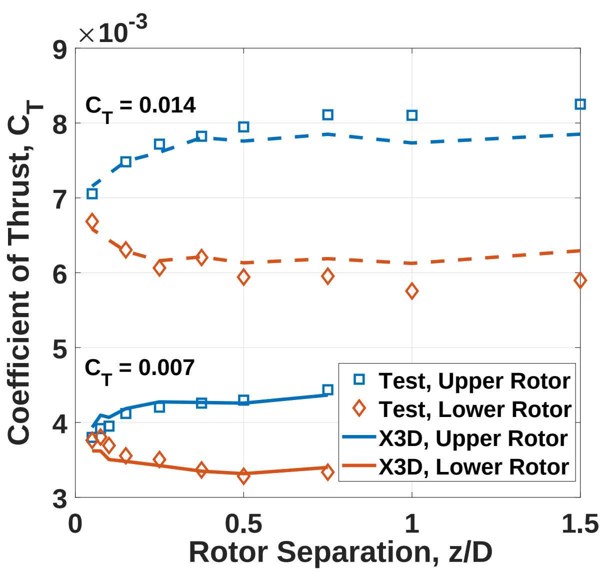

Figure 15: Upper and lower rotor thrust coefficient in hover versus various rotor separation distances for two thrust conditions.

I3D COUPLING METHODOLOGY

The I3D coupling methodology employed here is the CFD/CA delta-coupling procedure unique to rotorcraft trim solution (Refs. 32–34) extended recently to 3-D structures (Ref. 24). A 3D–to–1D interface, defined as level I (Ref. 29), is used here to allow the existing CFD beam-based mesh motion and 2-D sectional airloads post-processing to be utilized. The level I interface uses the 1-D lifting-line to exchange deformations and airloads but still accounts for the 3-D forcing of the structure. The assumptions are clarified below.

To pass structural deformations from X3D to CFD, the 3-D blade deflections are reduced to a 1-D beam-like description at the $1/4$-chord. This is accomplished by using the relative positions of nodes at the leading and trailing edges (that define the chord), and upper and lower surfaces (that define the thickness) to extract beam-like deformations in terms of three translations (u, v, w) and three rotations $(\theta_x, \theta_y, \theta_z)$ for each blade section. Thus, the true deflections are not passed to CFD mesh motion, but only the beam-like deformations, which are exact only when there are no cross-sectional deformations.

To return airloads to X3D, CFD integrates the pressure and shear into segmental normal and chord and pitching moments about $1/4$-chord — a procedure that is already available and validated. But these should not be imposed on the 3-D structure. The airloads must be distributed into nodal forces over all the surface nodes of the structural mesh. This distribution again follows an assumption. It is assumed the normal force on the surface varies linearly with its chordwise coordinate, and the in-plane force on the surface varies quadratically with its thickness coordinate. The variation is found exactly by ensuring the pitching moments remain intact. Thus, the surface forcing is a gross approximation of true forcing, but at least retains the same fidelity as the airloads.

For a given node, the nodal forces are assumed to be

$$f_N = \alpha_0 + \alpha_1 \varepsilon; \qquad f_C = \alpha_2 + \alpha_1 \eta^2 \tag{2}$$

where f_N and f_C are the normal and in-plane forces respectively, ε and η are the chordwise and thicknesswise position of the node, and $\alpha_0, \alpha_1, \alpha_2$ are three coefficients to be solved for all nodes. The total segmental airloads are obtained from the sum of nodal forces as given in Eq. 3. The axial nodal force is ignored unless axial airloads are supplied, but these normally are negligible.

$$F_N = \sum f_N; \quad F_C = \sum f_C; \quad M_{25} = \sum (f_N \varepsilon - f_C \eta); \tag{3}$$

For a total of n surface nodes, the total segmental airloads should be equal to the assumed distribution. This is given by Eq. 4. The coefficients are then evaluated by inverting the matrix. This methodology allows for the total forces and moments to be conserved.

$$\begin{bmatrix} F_N \\ F_C \\ M_{25} \end{bmatrix} = \begin{bmatrix} n & \sum \varepsilon & 0 \\ 0 & \sum \eta^2 & n \\ \sum \varepsilon & \sum(\varepsilon^2 - \eta^3) & -\sum \eta \end{bmatrix} \begin{bmatrix} \alpha_0 \\ \alpha_1 \\ \alpha_2 \end{bmatrix} \tag{4}$$

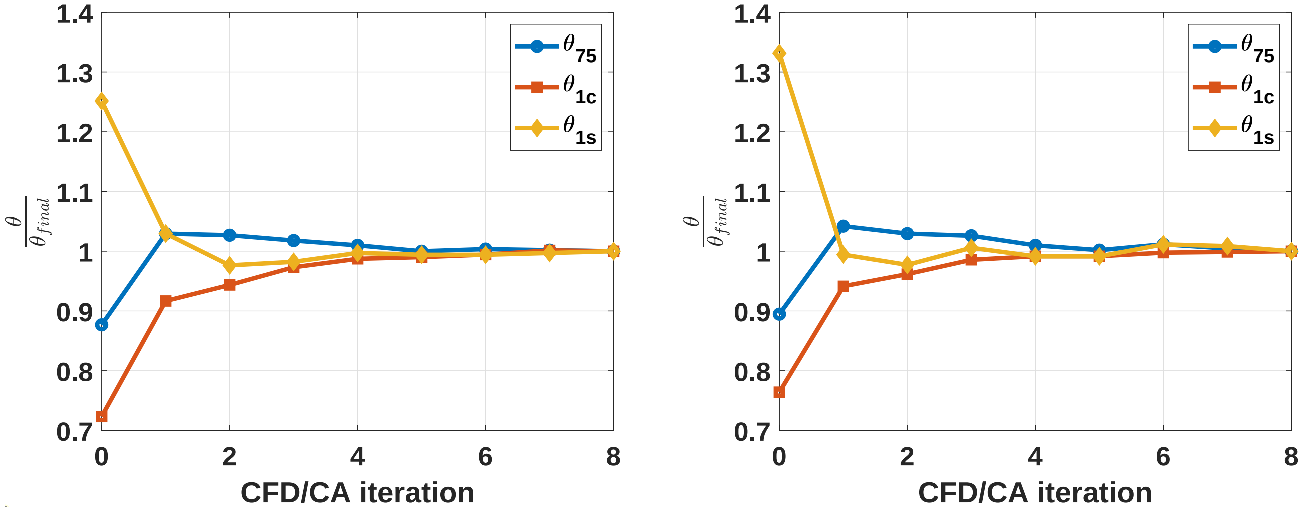

(a) Upper rotor (b) Lower rotor

Figure 16: 3-D CFD/CA coupling convergence of trim controls at $\mu = 0.1$, $C_T/\sigma = 0.08$.

LOW SPEED

The low-speed transition flight is analyzed first to verify results published recently by Sikorsky (Refs. 9, 21). The Sikorsky conditions were unavailable, except for a speed of 37 knots. Based on the rotor parameters, this corresponded to an advance ratio of $\mu = 0.1$. A forward shaft tilt of $\alpha = -2^\circ$ is assumed, and a blade loading of $C_T/\sigma = 0.08$.

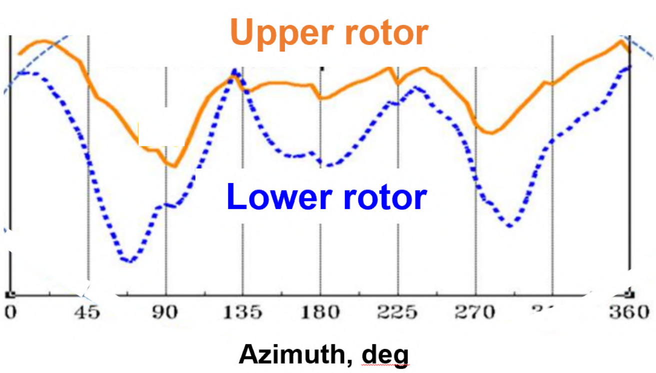

Figure 17: Sikorsky predicted S-97 blade lift in low-speed flight (Ref. 21); exact r/R, α or C_T/σ are unpublished.

Trim Controls

Figure 16 shows that the trim controls converge easily. Eight coupling iterations cover a total of 24 revolutions of CFD. The collectives are identical between the rotors. The lower rotor requires a slightly higher θ_{1c} due to wake interactions affecting lateral flapping. These are listed in Table 3.

Table 3: Converged trim controls at $\mu = 0.1$

Trim control	Upper rotor	Lower rotor
θ_{75}	6.42°	6.42°
θ_{1c}	4.06°	4.78°
θ_{1s}	-1.93°	-2.00°

Airloads

The predicted S-97 airloads published by Sikorsky in Ref. 21 is shown in Figure 17. The predictions used coupled CFD-CSD with a beam-based structural model. The predicted normal force ($\approx$ lift) of the present work is shown in Figure 18. The local azimuth of each rotor is used for comparing the airloads. The lower rotor has higher harmonics of 3-5/rev. Even though the Sikorsky airloads did not have axes labels, so the magnitudes could not be verified, the fundamental trends are similar – the upper rotor carries higher steady loading, whereas the lower rotor carries higher oscillatory loading.

To obtain fundamental insights, the Hooper plots are constructed in Figure 19. The vortex intertwining is reinforced by the ingestion of the upper rotor wake into the lower rotor, and these reinforced vortices being closer to the lower rotor produces magnified impulses in the first and fourth quadrants of the lower disk. The first impulse is severe enough to drive the 20% of the tip into negative lift, thereby complicating the roll-up further.

The 8/rev impulsive loading due to blade crossing is a minor issue that is insignificant. What is interesting is that they are stronger in pitching moments shown in Figure 20. Unlike lift, the pitching moments are almost identical for upper and lower rotors, except for the impulses. The presence of these impulses in the pitching moment indicates these are more than mere bound circulation crossings and perhaps related to flows between the blades. This would clarify why they are not well-

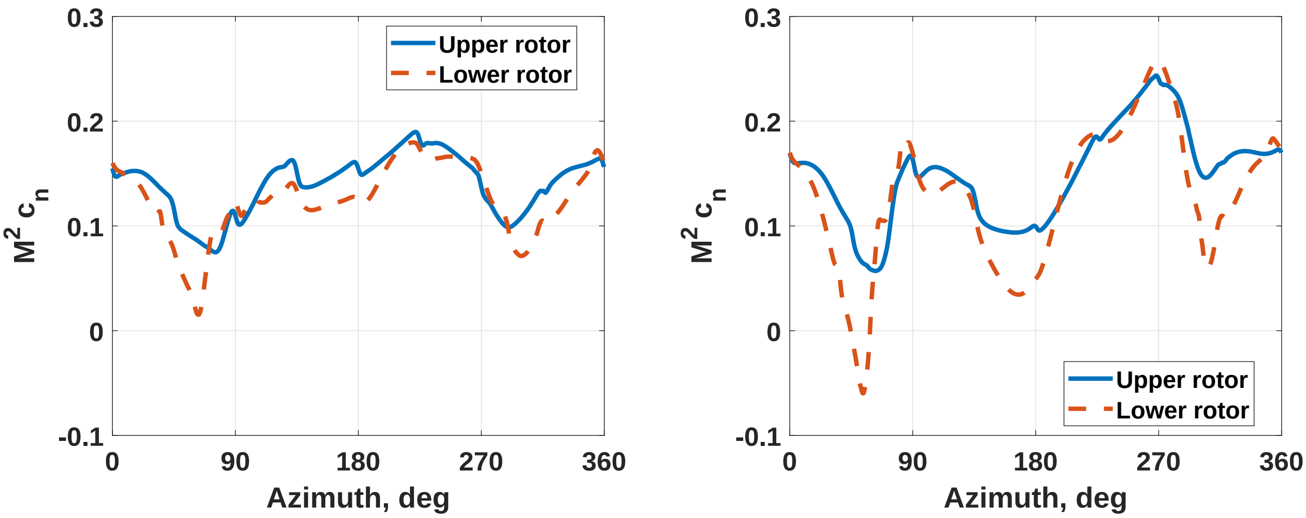

(a) 82.5% R (b) 93.5% R

Figure 18: Normal force distribution at $\mu = 0.1$, $C_T/\sigma = 0.08$ for two radial stations.

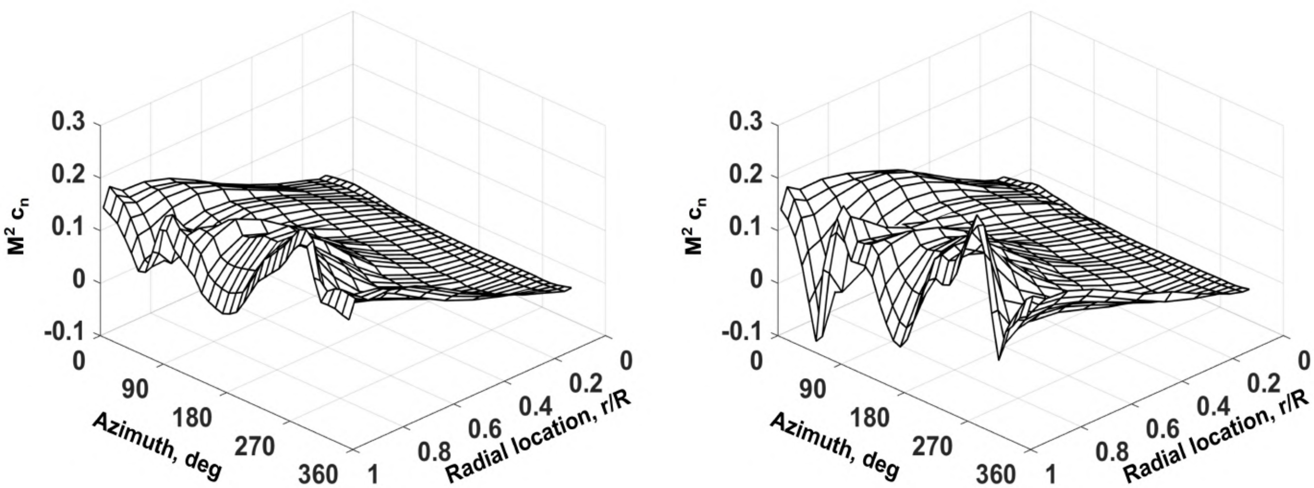

(a) Upper rotor (b) Lower rotor

Figure 19: Normal force Hooper plots for upper and lower rotors at $\mu = 0.1$, $C_T/\sigma = 0.08$.

predicted by lifting-line models. In the end, they are very high-frequency impulses of 8-48/rev and hence do not affect structural loads. They are, at best, an academic curiosity.

Figures 21a and 21b show the vorticity field. The tip vortices from the upper rotor are distinct. The tip vortices from the lower rotor on the advancing side are less so due to the negative lift. The positive vortex likely moves inboard with a weaker sheet outboard of reverse rotation, causing turbulent structures. Further, disruption is caused by the upper wake impingement. The result is that the lower rotor is hammered by oscillatory loading even when carrying a lesser trim burden. The upper rotor wake hits the rear disk of the lower rotor (seen from Figure 21b) – resulting in magnified impulses in the lower rotor airloads.

3-D Stresses

Figure 22 shows the axial (bending) stresses (σ_{11}). The blade skin is peeled off to visualize the internal stresses. The maximum bending stress is carried by the spar, obviously with compression on the top and tension at the bottom. On first inspection, it would appear that the bending is primarily characterized by the first mode. The azimuthal variation of maximum tensile and compressive stresses is shown in Figure 23. For both rotors, they occur on the spar near the root. The stress variation is dominantly 3/rev, with significant contributions from 4 and 5/rev. This indicates the second mode is equally important. All the interactions and complications observed in airloads are passed on to the stresses. The upper rotor absorbs the maximum steady tensile and compres-

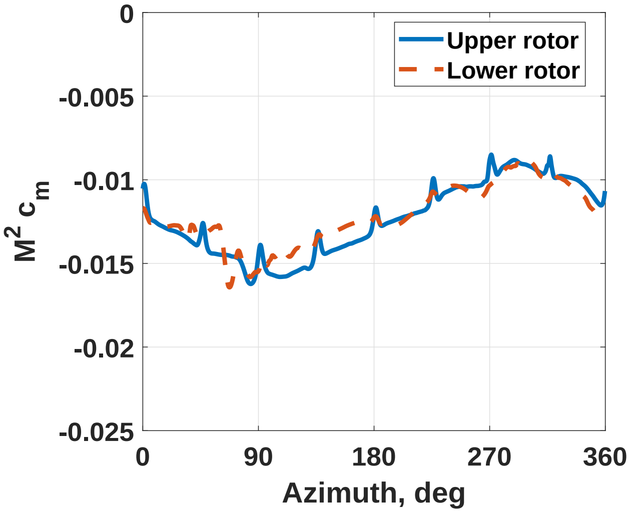

(a) 82.5% R

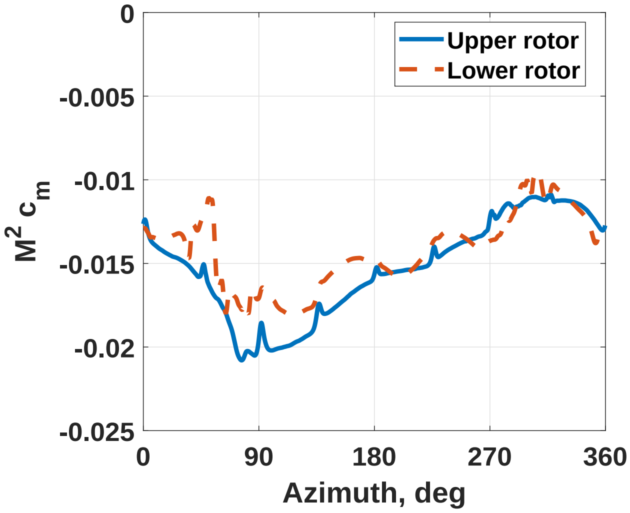

(b) 93.5% R

Figure 20: Pitching moment distribution at $\mu = 0.1$, $C_T/\sigma = 0.08$ for two radial stations.

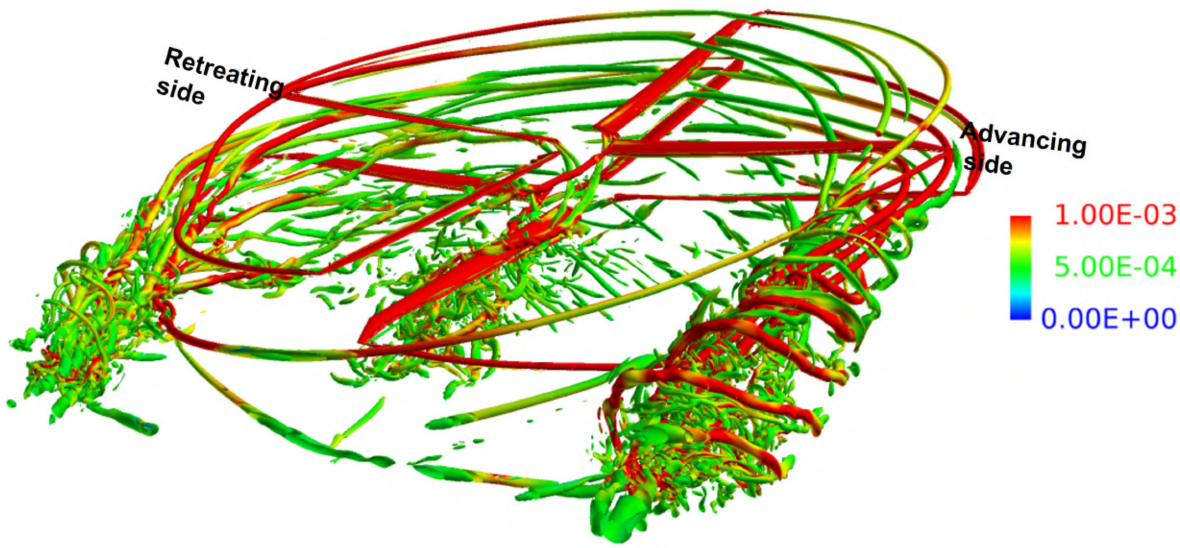

(a) Isometric View

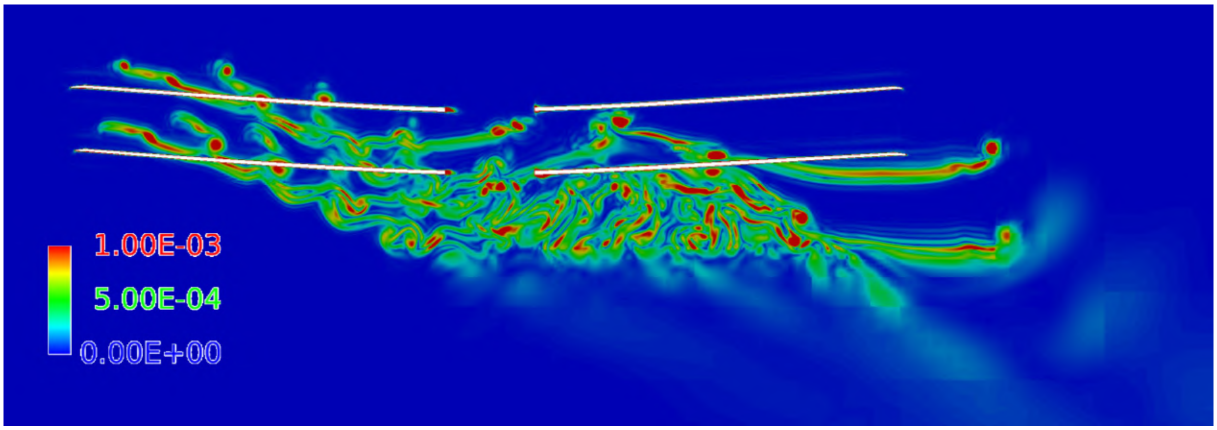

(b) Side View

Figure 21: Converged 3-D CFD flow field in isometric and side view at low-speed flight, $\mu = 0.1$, $C_T/\sigma = 0.08$; iso-surface of Q-criterion, 0.001, colored by vorticity.

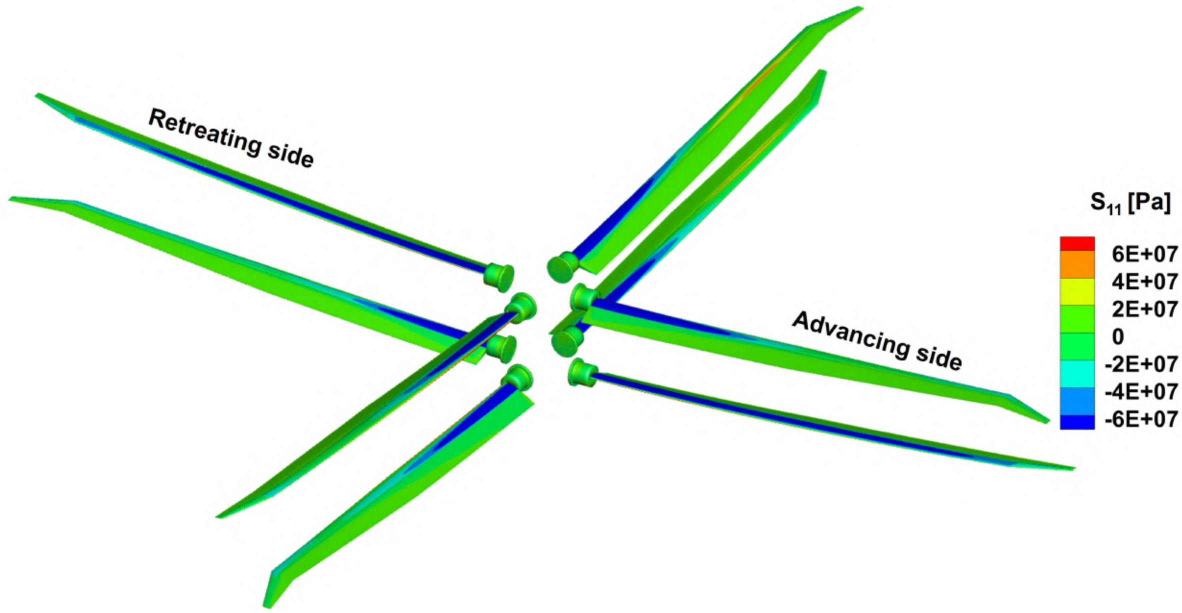

Figure 22: Axial/bending stress distribution at low-speed flight, $\mu = 0.1$, $C_T/\sigma = 0.08$.

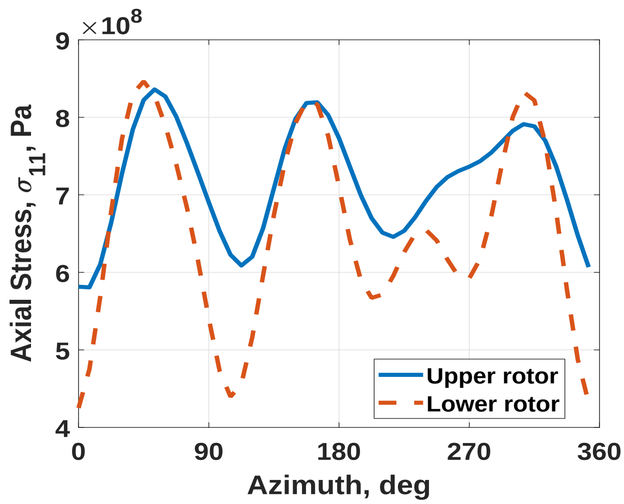

(a) Tensile stress – top

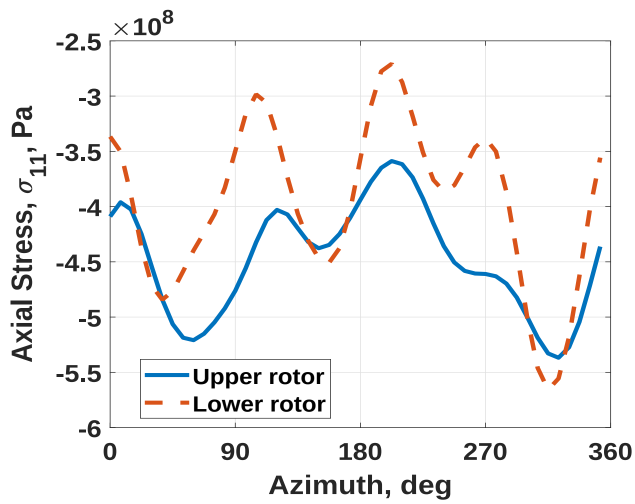

(b) Compression stress – bottom

Figure 23: Maximum tensile and compressive stresses versus azimuth at $\mu = 0.1$, $C_T/\sigma = 0.08$.

sive stresses. But it is the lower rotor that is hammered with oscillatory stresses. This includes higher 4/rev, hence a greater participation of the second mode.

If the stresses (strains, really) were to be measured in flight with a flap-bending strain gauge, what would be picked up is the differential between the bottom and the top of the spar. It is instructive to see this variation. Figure 24 shows this variation, and the nodes corresponding to top and bottom of the spar are highlighted. First, unlike airloads, the maximum variation is at the root end. Second, unlike airloads, they remain in phase from root to tip, showing a clearly dominant 3/rev behavior with some 4-5/rev. This is also seen in Figure 25, which shows the differential spar stresses along the span for two azimuths. There is a slight rise in stress concentration near the tip ($\approx 90\%R$), where the swept tip starts. The gradual drop in the stresses at the tip ($> 92\%R$) is due to a decrease in spar thickness as the plies are reduced in this region for a lower chord.

HIGH SPEED

The advance ratio is now increased to $\mu = 0.35$, corresponding to 150 knots. The actual aircraft will likely fly at a different shaft angle and reduce rotor tip speed. It is also likely to carry non-zero net hub pitch and roll

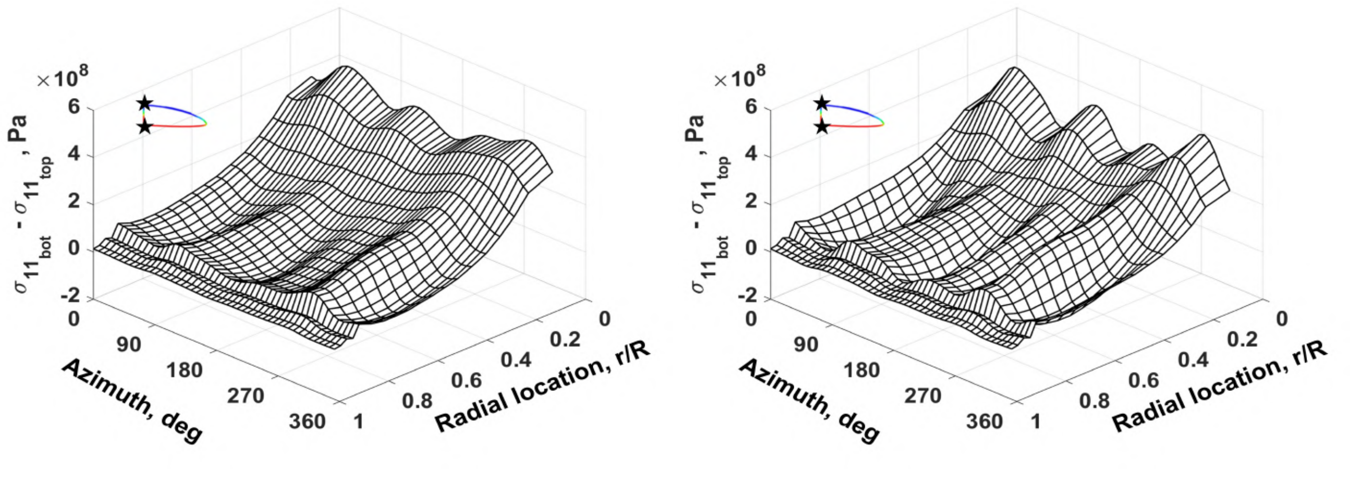

(a) Upper rotor

(b) Lower rotor

Figure 24: Differential blade spar stresses (bottom - top) for upper and lower rotors at $\mu = 0.1$, $C_T/\sigma = 0.08$.

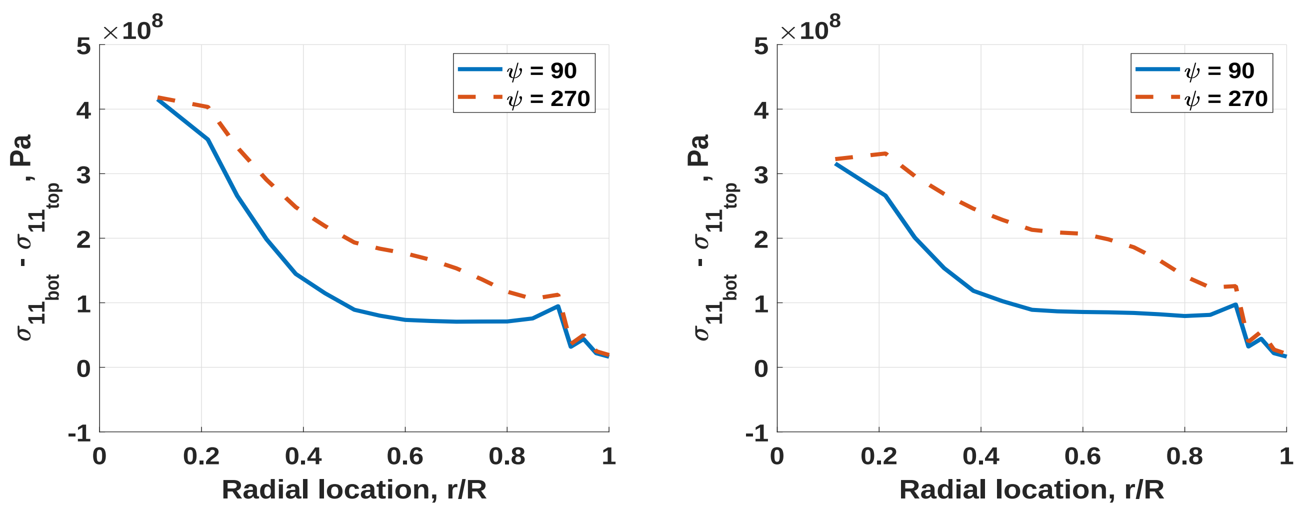

(a) Upper rotor

(b) Lower rotor

Figure 25: Differential blade spar stresses (bottom - top) versus span at $\psi = 90^\circ$ and 270° for $\mu = 0.1$, $C_T/\sigma = 0.08$.

moments to counter the effect of pusher prop and aircraft center of gravity travel. These complications are not warranted in the absence of actual aircraft data.

Trim Controls

The trim controls again converged easily in eight iterations over a total of 20 CFD revolutions. The collectives now differ slightly between the rotors. The lateral cyclic is lowered in the absence of the wake. The longitudinal cyclic is raised for the balance of hub pitch moments.

Table 4: Converged trim controls at $\mu = 0.35$

Trim control	Upper rotor	Lower rotor
θ_{75}	6.01°	6.38°
θ_{1c}	1.83°	2.06°
θ_{1s}	-5.57°	-6.01°

Airloads

The predicted normal force (≈ lift) distribution over span and azimuth is shown in Figure 26. In the absence of wake interactions, the upper and lower rotors show similar lift. A large negative lift is seen near the advancing tip to balance the roll moment.

The azimuthal variation of blade normal force at two radial stations ($82.5\%R$, $93.5\%R$) are shown in Figure 27. The oscillatory lift near the tip is dominated by 1-2/rev harmonics, unlike at low speed. The dominant feature is the up-down impulse in the first quadrant from inboard wake interaction from the negative lift. The 8/rev impulsive loading due to blade crossing is visible at $82.5\%R$, but once again, it is a minor effect. The pitching moment variation over azimuth is shown in Figure 28. Near the tip of the advancing side, there appears to be a spike in the pitching moment (Figures 28a and 28b). Figure

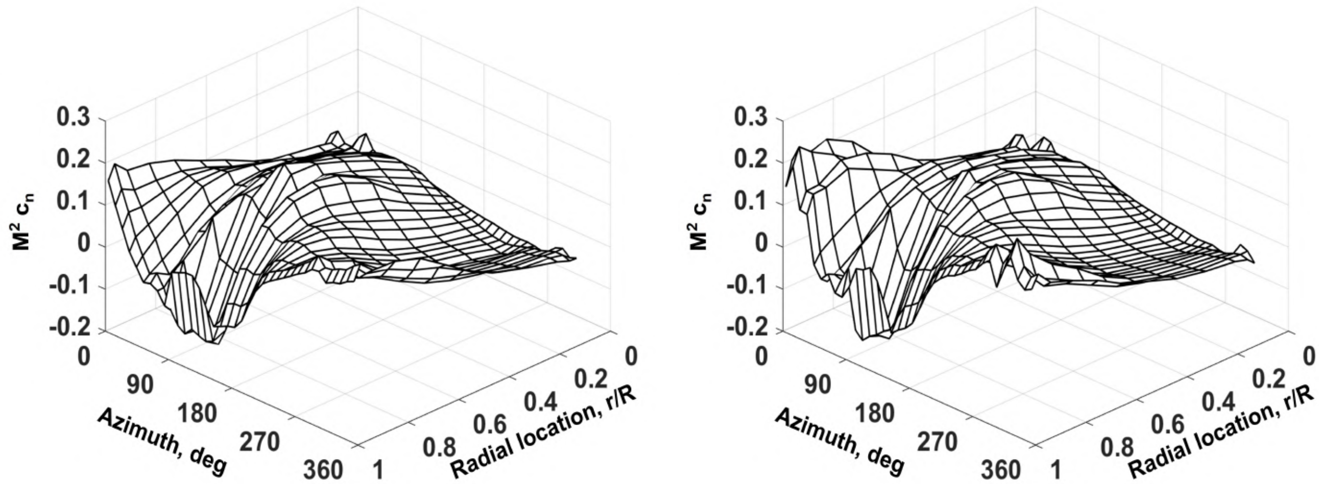

(a) Upper rotor (b) Lower rotor

Figure 26: Normal force Hooper plots for upper and lower rotors at $\mu = 0.35$, $C_T/\sigma = 0.08$.

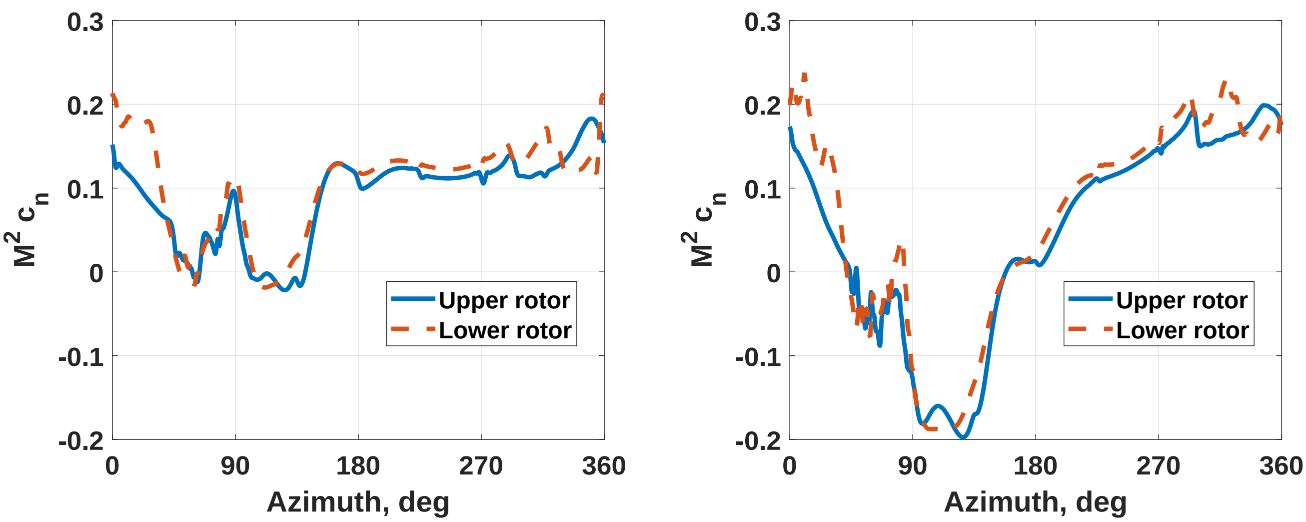

(a) 82.5% R (b) 93.5% R

Figure 27: Normal force distribution at $\mu = 0.35$, $C_T/\sigma = 0.08$ for two radial stations.

29 shows the pressure coefficient along the blade at the advancing side ($\psi = 90°$). There is not much difference between upper and lower rotors. Near the root, there is suction on the upper surface but the flow field is benign. Near the tip, unsteady shocks form. Note the advancing tip Mach number is 0.875. The shock first appears on the upper surface around $85\%R$ and then on both upper and lower surfaces toward the tip. These cause high unsteady pitching moments due to the shift in the aerodynamic center and also increases the drag. To study the chordwise location of the shock, Figure 30 shows the pressure coefficient distribution along the chord at radial stations $83\%R$ and $98\%R$. The upper and lower rotors show identical behavior. Shock formation on the upper surface is confirmed from Figure 30a, and on the lower surface from Figure 30b.

Figures 31a and 31b show the vorticity field. The intertwinning is not visible as the wake is washed back. Instead, two vortices are released from every blade, one from the tip, and the other around $80-90\%$ R, where the blade lift passes through zero. The second vortex hits the following blade resulting in the first quadrant impulse. There is no rotor-to-rotor wake interaction in front of the disk nor on the advancing or retreating sides as seen in Figure 31b.

3-D Stresses

Figure 32 shows the axial (bending) stresses (σ_{11}). The blade skin is peeled off to visualize the internal stresses. The stresses show 3-D patterns. Unlike low speed, near mid-span, tension is seen on the top and compression

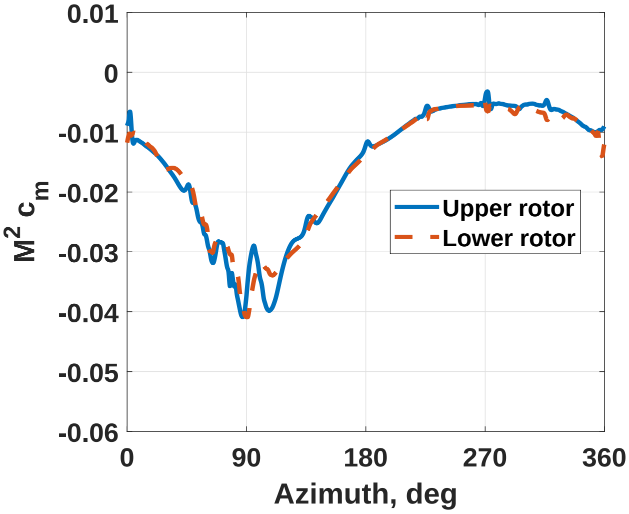

(a) 82.5% R

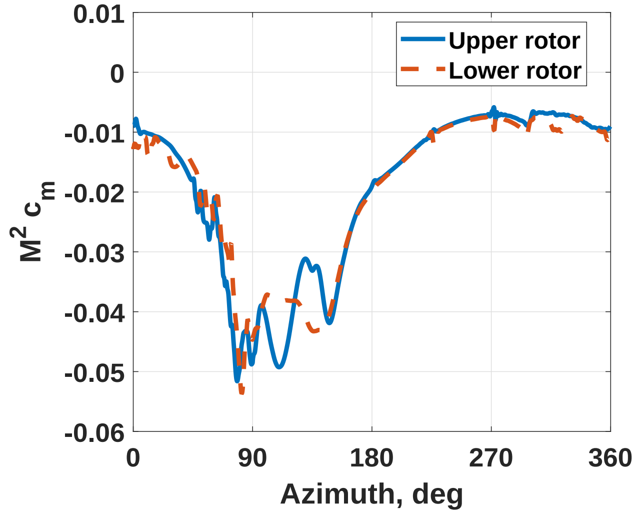

(b) 93.5% R

Figure 28: Pitching moment distribution at $\mu = 0.35$, $C_T/\sigma = 0.08$ for two radial stations.

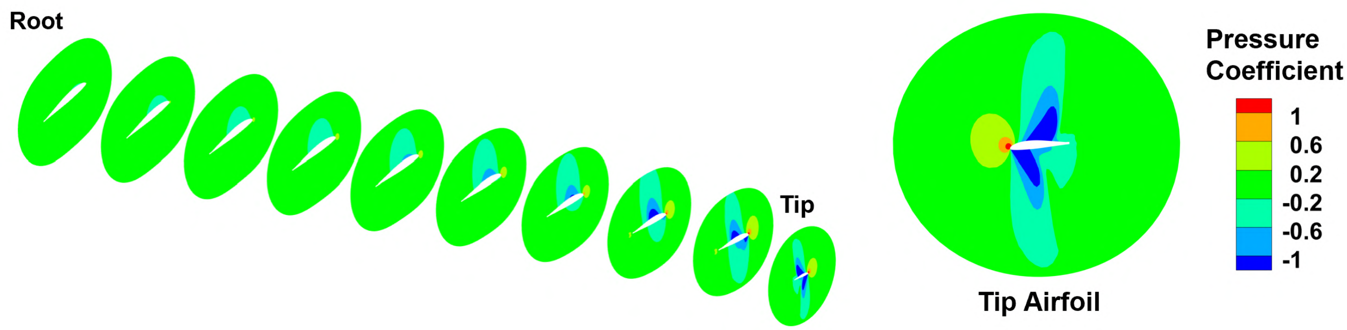

(a) Upper rotor

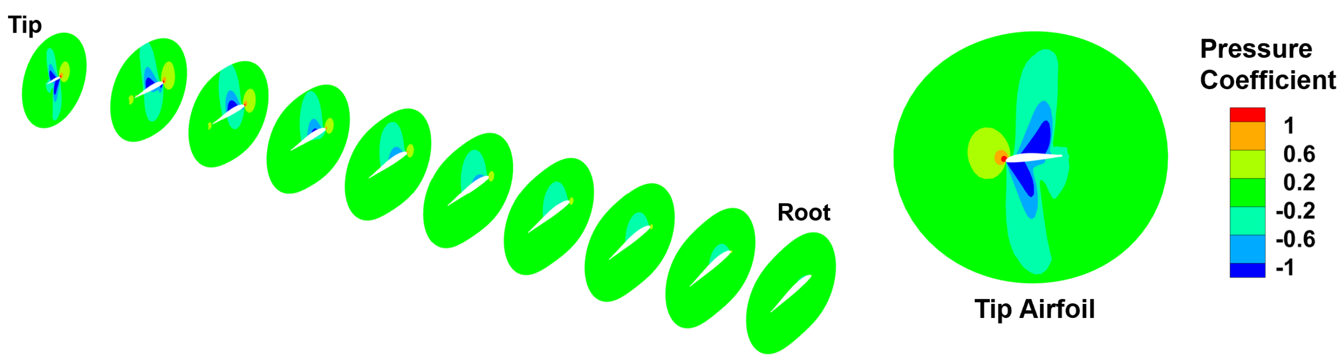

(b) Lower rotor

Figure 29: Pressure coefficient distribution on airfoil along the blade advancing side at $\mu = 0.35$ highlighting the formation of shock near the tip.

on the bottom, indicating the presence of the second blade bending mode.

The azimuthal variation of maximum tensile and compressive stresses is shown in Figure 33. Unlike the low-speed flight, the upper and lower rotors have a very similar distribution, characterized by a 2/rev behavior. The upper rotor and lower rotor have similar stresses in tension and compression, with the lower rotor having a slightly higher magnitude. These are of the same order of magnitude when compared to the low-speed flight. This implies that the oscillatory stresses at low speed are just as critical as at high speed, although the vibratory stresses 3-5/rev are lower. This can be attributed to the stiff in torsion blades without significant elastic twist.

Figure 34 shows the differential blade spar stresses over the entire rotor disk. The stresses are maximum near

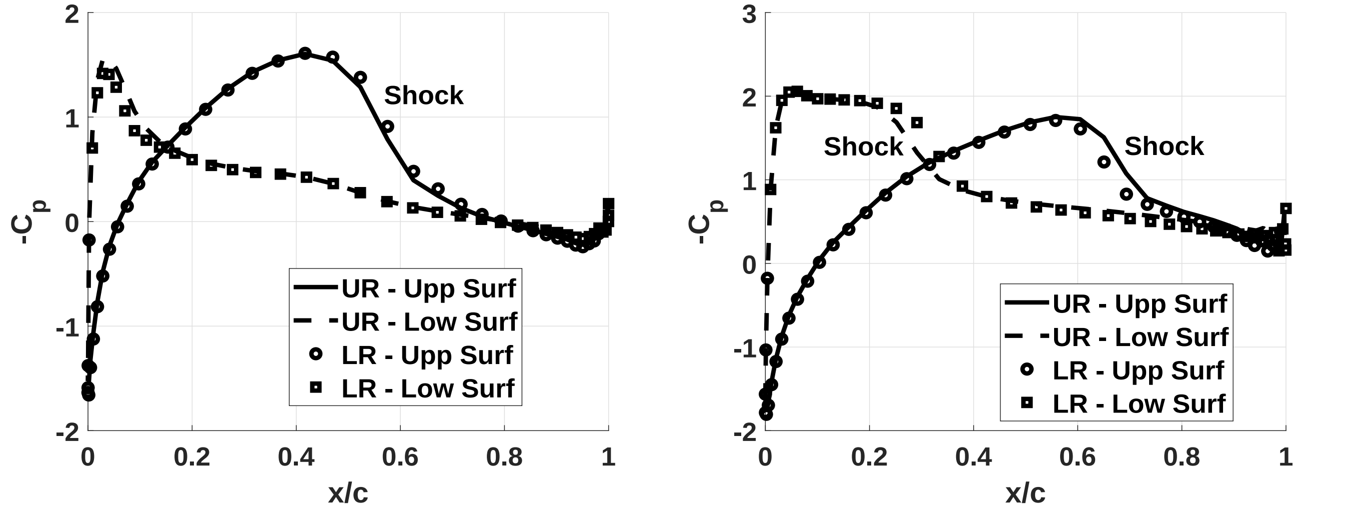

(a) 83 % R (b) 98 % R

Figure 30: Pressure coefficient distribution along airfoil at different spanwise locations of advancing side ($\psi = 90°$) in high-speed flight $\mu = 0.35$.

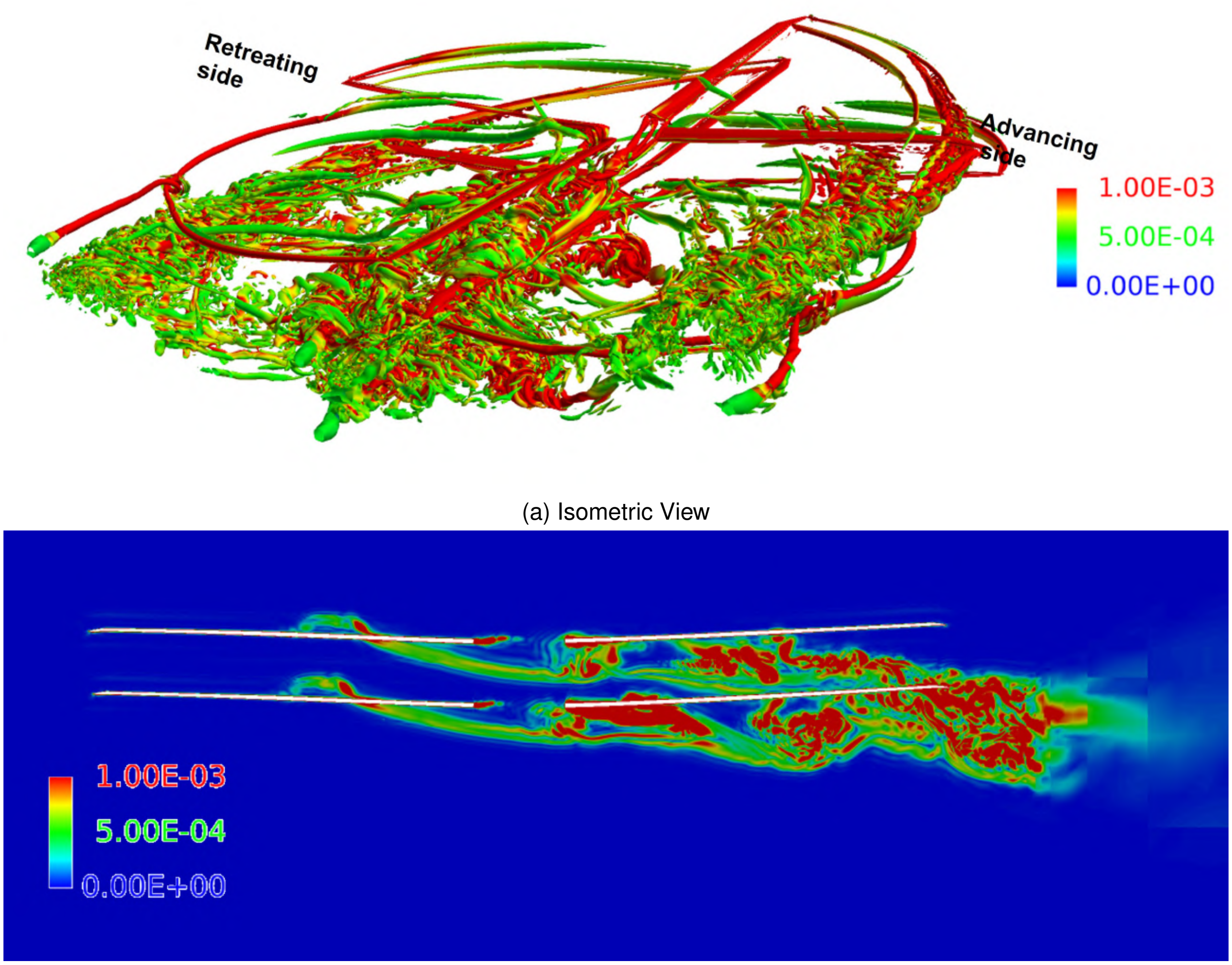

(a) Isometric View

(b) Side View

Figure 31: Converged 3-D CFD flow field in isometric and side view at high-speed flight, $\mu = 0.35$, $C_T/\sigma = 0.08$; iso-surface of Q-criterion, 0.001, colored by vorticity.

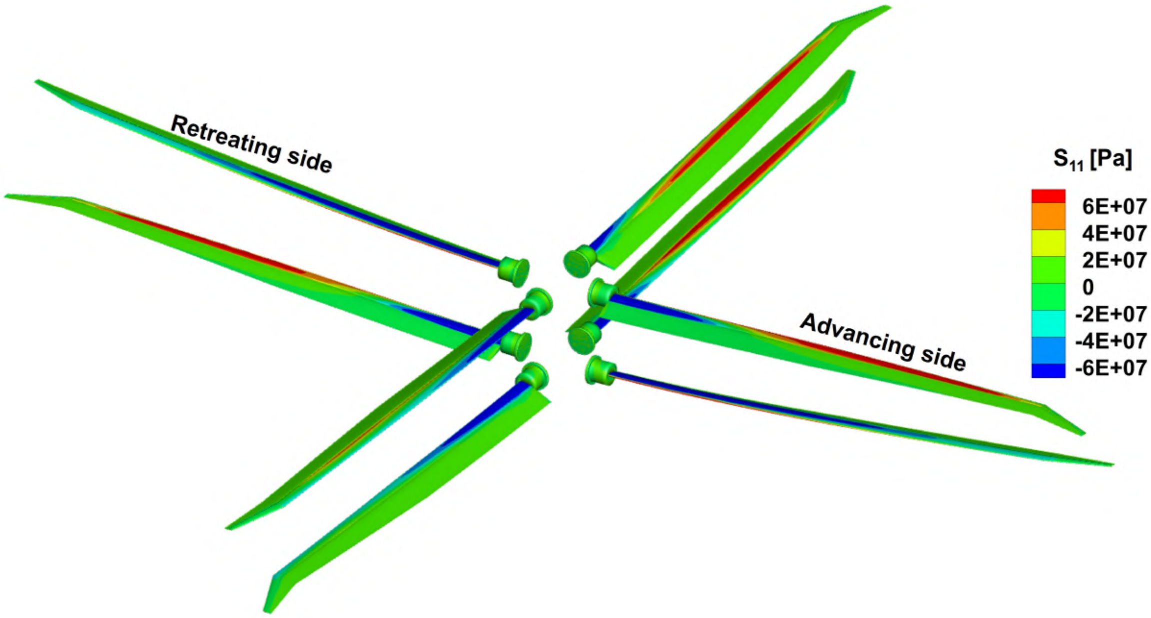

Figure 32: Axial/bending stress distribution at high-speed flight, $\mu = 0.35$, $C_T/\sigma = 0.08$.

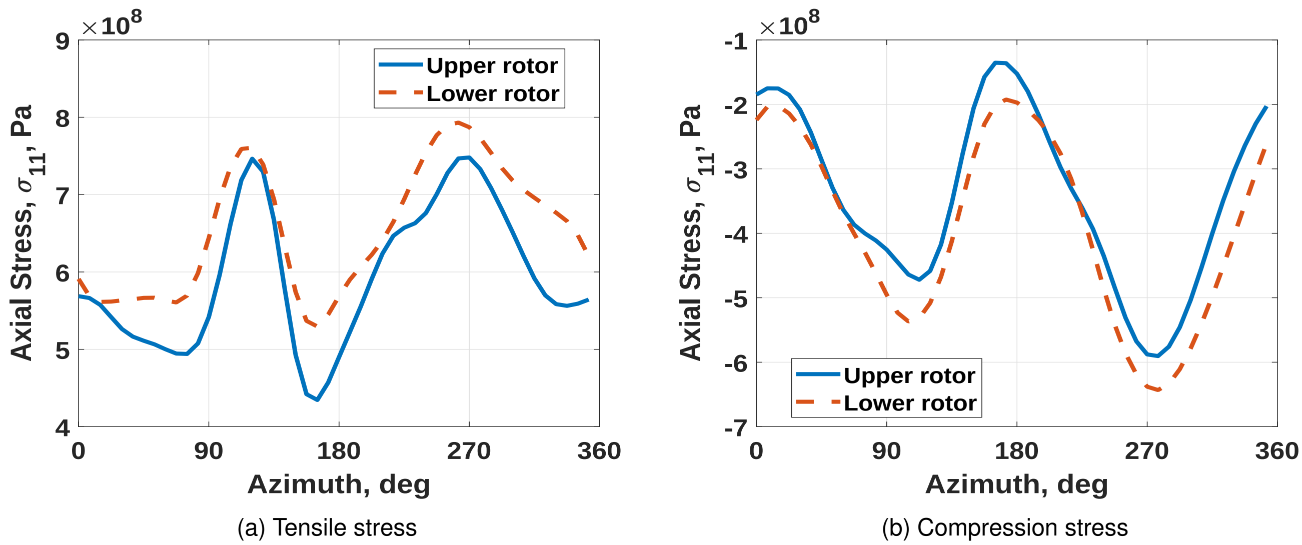

Figure 33: Maximum tensile and compressive stresses versus azimuth at $\mu = 0.35$, $C_T/\sigma = 0.08$.

the root naturally, but unlike low speed, they decrease only until mid-span and then increase. They become negative near the mid-span, denoting the presence of both the first and second bending modes. This is confirmed in Figure 35, which shows the differential spar stresses along the span. At $\psi = 270°$, the variation indicates the first mode, whereas, at $\psi = 90°$, both the first and second modes are evident. This is due to the large negative lift near the advancing side of the blades.

VERY HIGH SPEED

The advance ratio is now further increased to $\mu = 0.5$, corresponding to 220 knots. The rotor can no longer be trimmed without lift offset (LO). A minimum LO of $10\%R$ is used. The actual aircraft will likely fly at a $20-25\%R$ LO, perhaps at a lower tip speed, with a pusher prop, to alleviate the loads, but the objective here is to stress test the methodology.

Trim Controls

The convergence of trim controls now requires some relaxation. The convergence of the coupling is more difficult due to very high advancing tip Mach number ($M_{ADV} = 0.975$), which deviates the lifting line airloads dramatically from CFD. Table 5 lists the converged control angles. The upper rotor has a higher collective and longitudinal cyclic. The lateral cyclic is the same for both rotors.

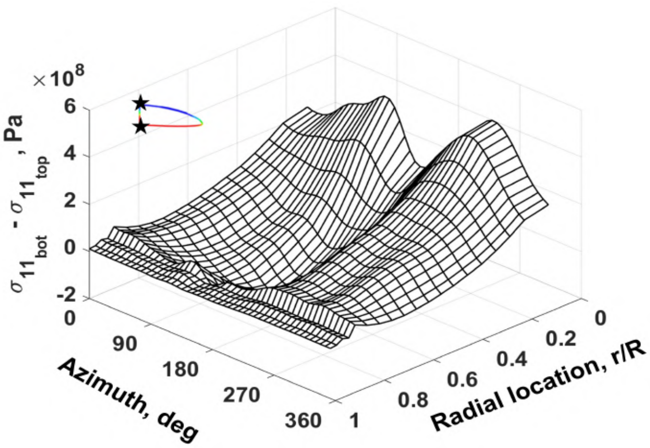

(a) Upper rotor

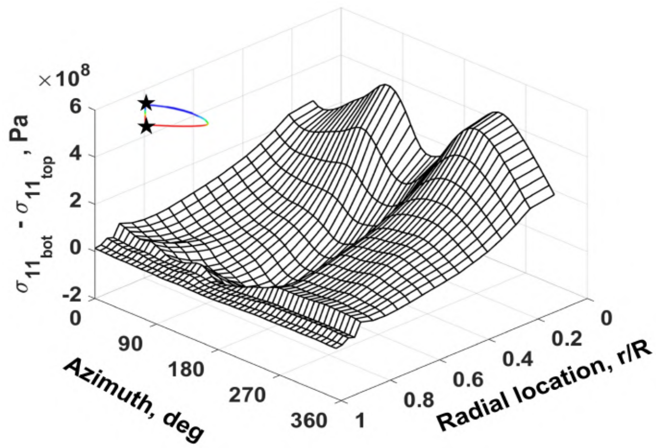

(b) Lower rotor

Figure 34: Differential blade spar stresses (bottom - top) for upper and lower rotors at $\mu = 0.35$, $C_T/\sigma = 0.08$.

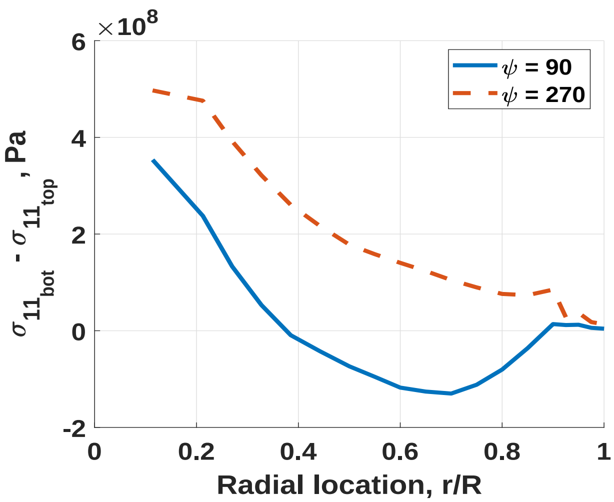

(a) Upper rotor

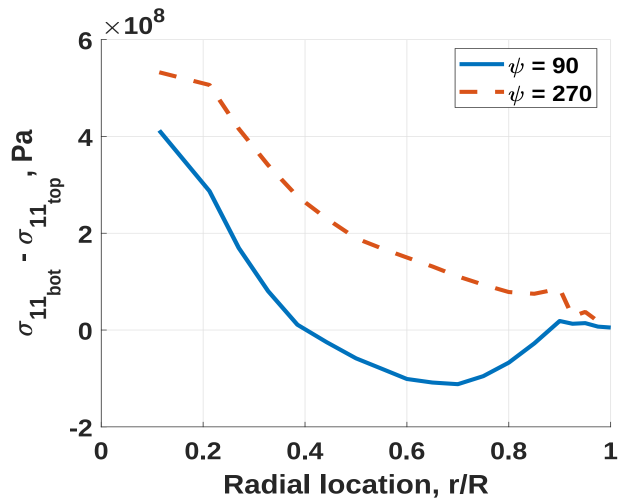

(b) Lower rotor

Figure 35: Differential blade spar stresses (bottom - top) versus span at $\psi = 90°$ and $270°$ for $\mu = 0.35$, $C_T/\sigma = 0.08$.

Table 5: Converged trim controls at $\mu = 0.5$

Trim control	Upper rotor	Lower rotor
θ_{75}	8.96°	6.15°
θ_{1c}	2.79°	2.79°
θ_{1s}	-6.86°	-5.18°

Airloads

The predicted normal force ($\approx$ lift) distribution over span and azimuth is shown in Figure 36. There is more disparity between the upper and lower rotor compared to the previous high-speed case, and is consistent with the trim controls with lift offset. The waveform is similar on the inner half of the disk $r/R < 0.5$, but the lower rotor has a higher harmonic content on the outer half. There is a substantial negative lift on both rotors to produce an individual roll moment to achieve the targetted lift offset.

The azimuthal variation at two radial stations is shown in Figure 37. Harmonic analysis showed the upper rotor has a distinct 4/rev, in addition to the 1-2/rev content, whereas the lower rotor showed a greater 5/rev. The 8/rev impulsive loading due to blade crossing is barely visible and hence unimportant. The pitching moment and chord force over azimuth at different radial locations are shown in Figures 38 and 39, respectively. The spike in the pitching moment on the lower rotor near the tip is due to dramatic aerodynamic center movement caused by the shock. This behavior is similar on the upper rotor but less pronounced. In fact, the shock formed is so strong that the pitching moment sign is flipped momentarily. Particularly striking is the chord force which, because of wave drag, attains the same order of magnitude as the normal force (see Figure 39b).

The importance of transonic flow is shown in Figure 40. The pressure coefficient on the blade advancing side is plotted for upper and lower rotors. The shock first ap-

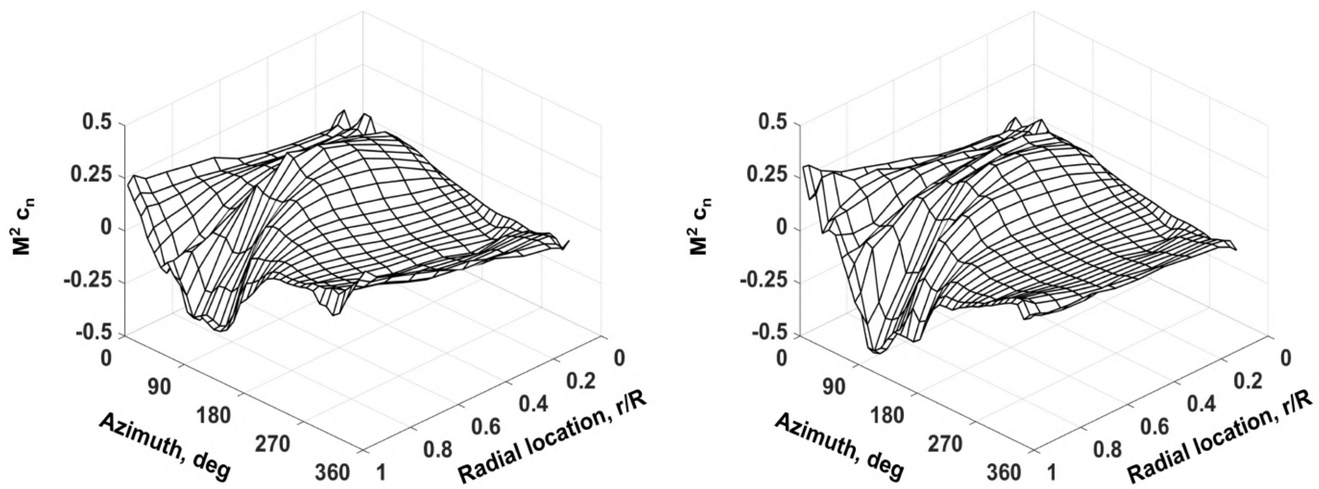

(a) Upper rotor (b) Lower rotor

Figure 36: Normal force Hooper plots for upper and lower rotors at $\mu = 0.5$, $C_T/\sigma = 0.08$.

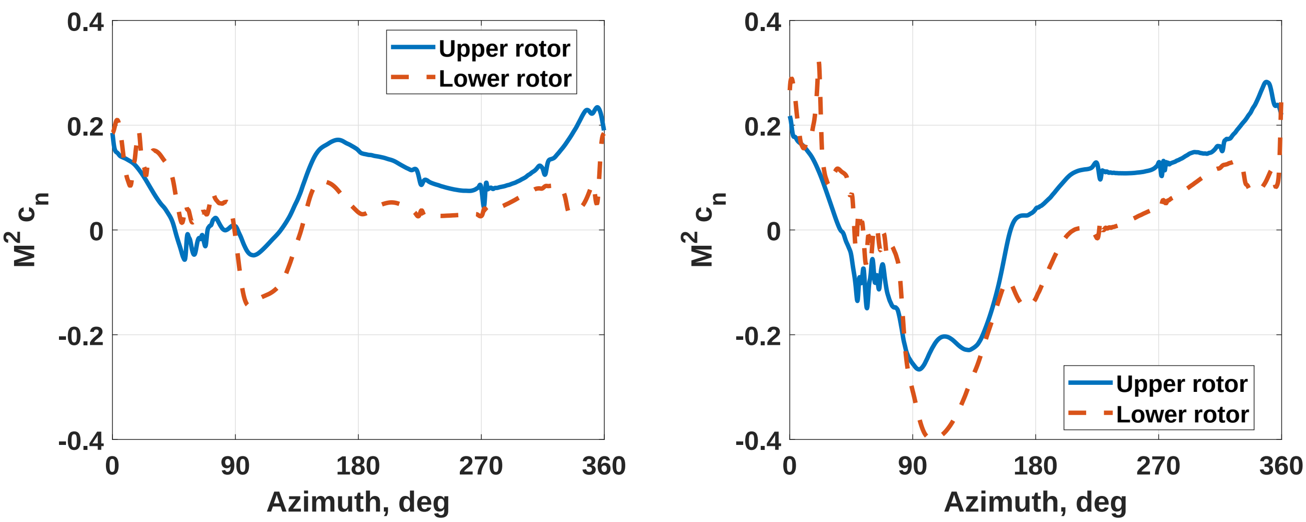

(a) 82.5% R (b) 93.5% R

Figure 37: Normal force distribution at $\mu = 0.5$, $C_T/\sigma = 0.08$ for two radial stations.

pears on the upper surface as inboard as $70\%R$, and then on the lower surface from around $80\%R$. Figure 41 shows the pressure coefficient along the airfoil chord. Between upper and lower rotors, there is not much difference in the pressure distribution at this azimuth; hence the airloads are similar.

Figures 42a and 42b show the wake. The wake is now even milder but with dual vortices on the advancing side more pronounced, consistent with the greater negative lift. Two vortices are released from every blade, one from the tip, and the other near where the blade lift passes to zero. The second vortex again hits the following blade resulting in the first quadrant impulse in airloads. There are even lesser inter-rotor interactions as seen in Figure 42b.

3-D Stresses

Figure 43 shows the axial (bending) stresses (σ_{11}). The blade skin is peeled off to visualize the internal stresses. Comparing with Figures 22 and 32 reveals clear differences in stress patterns for different flight speeds. The stresses vary even more in span and chord at this speed.

The maximum tensile and compressive stresses are shown in Figure 44 as before, but unlike before, now they occur at different locations on the blade. Figure 44 also specifies the location of the maximum stress. The stresses vary in a 3-D fashion. On the upper rotor, the maximum tensile stress occurs at the leading-edge bottom of the spar in the first quadrant, then the trailing-edge bottom of the spar in the second and third quad-

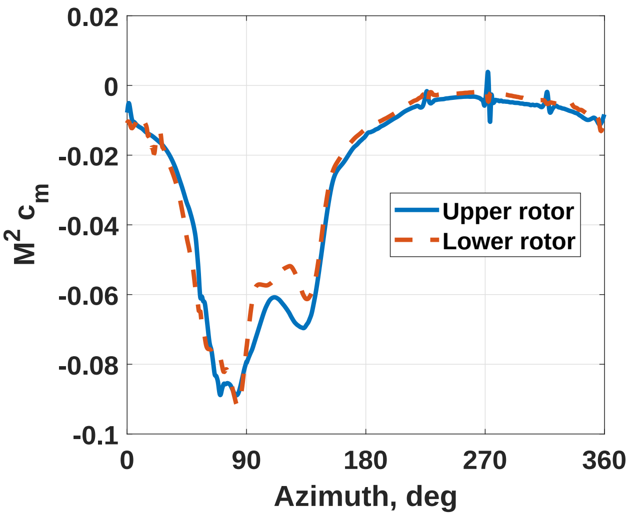

(a) 82.5% R

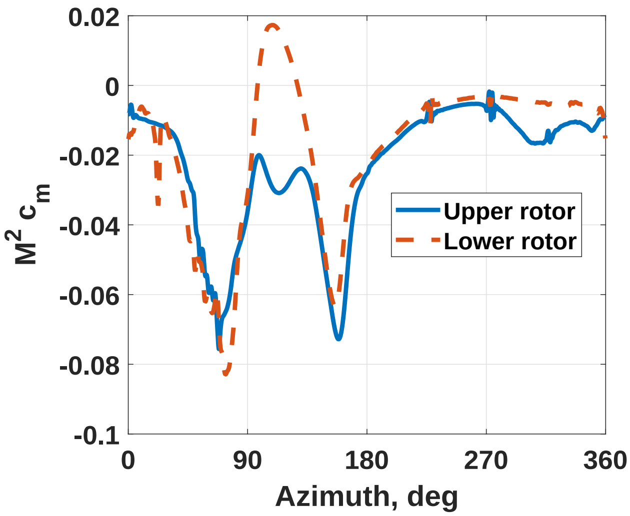

(b) 93.5% R

Figure 38: Pitching moment distribution at $\mu = 0.5$, $C_T/\sigma = 0.08$ for two radial stations.

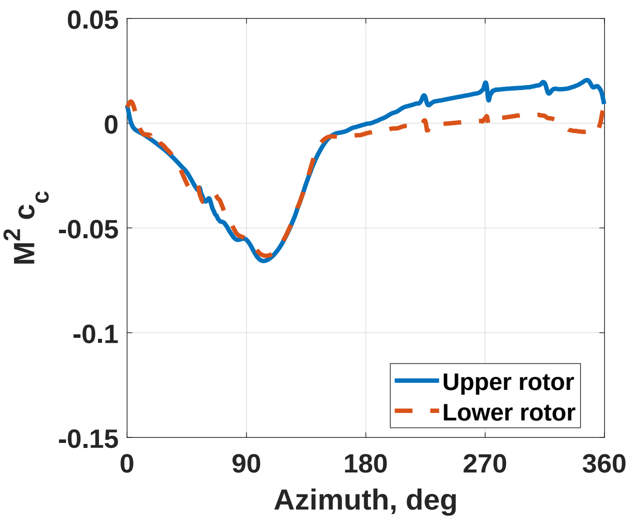

(a) 82.5% R

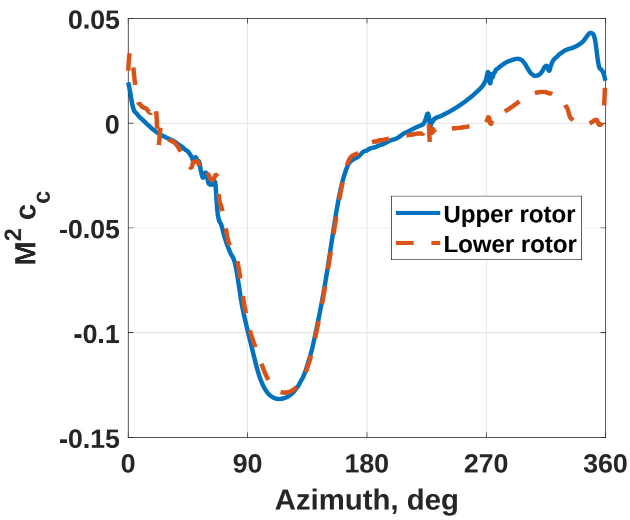

(b) 93.5% R

Figure 39: Chord force distribution at $\mu = 0.5$, $C_T/\sigma = 0.08$ for two radial stations.

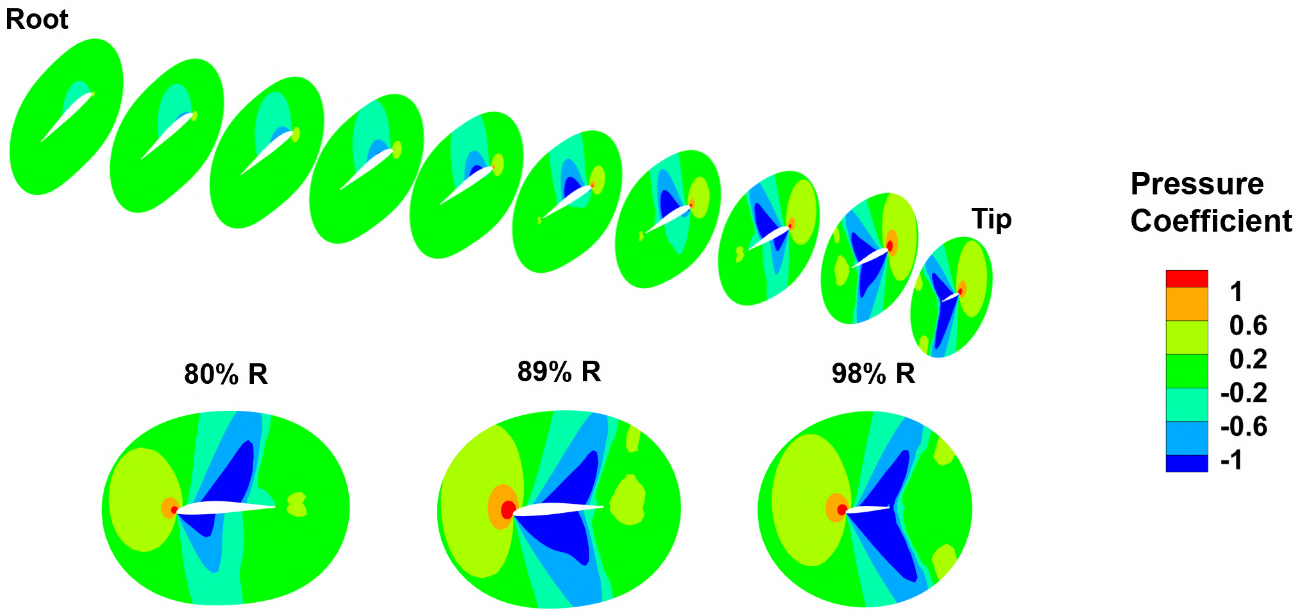

(a) Upper rotor

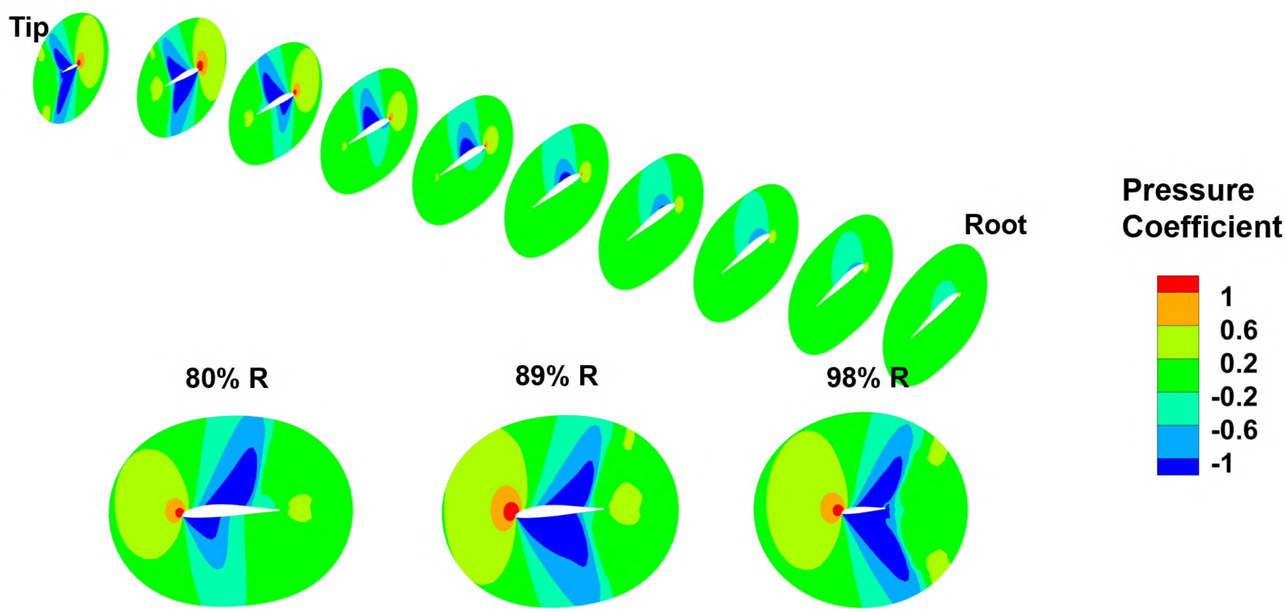

(b) Lower rotor

Figure 40: Pressure coefficient distribution on airfoil along the blade advancing side at $\mu = 0.5$ highlighting the formation of shock near the tip.

rants, and finally at the leading-edge bottom and trailing-edge top in the fourth quadrant. On the upper rotor, the maximum compression occurs at the trailing-edge top of the spar in the first quadrant, then the leading-edge top of the spar in the second quadrant, and finally at the leading-edge bottom and trailing-edge top in the fourth quadrant. The upper and lower rotors show different tensile and compressive stress patterns. On the lower rotor, the maximum tensile stress occurs at the trailing-edge bottom of the spar in the first quadrant, then the trailing-edge top of the spar in the second and third quadrants, and finally at the leading-edge bottom in the fourth quadrant. On the lower rotor, the maximum compression occurs at the trailing-edge top of the spar in the first and second quadrants, then the leading-edge bottom of the spar in the third quadrant, and finally, at

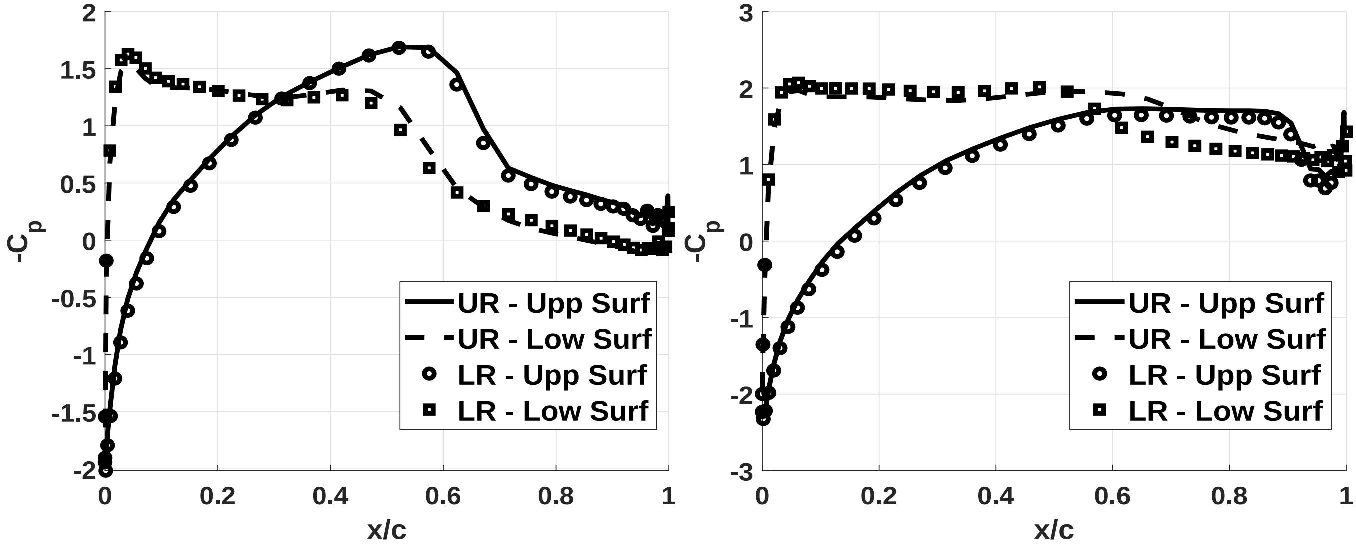

(a) 83 % R (b) 98 % R

Figure 41: Pressure coefficient distribution along airfoil at different spanwise locations of advancing side ($\psi = 90°$) in very high-speed flight $\mu = 0.5$.

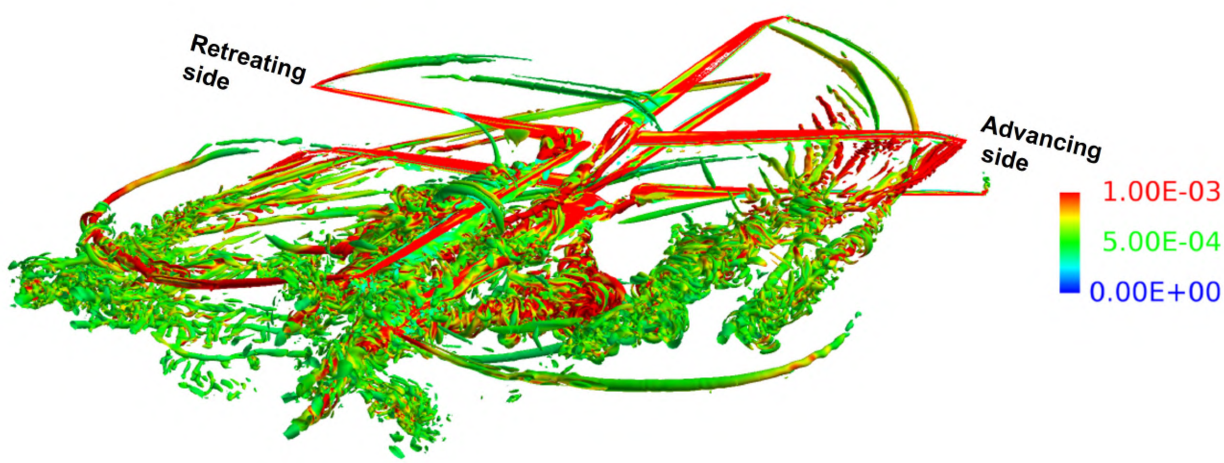

(a) Isometric View

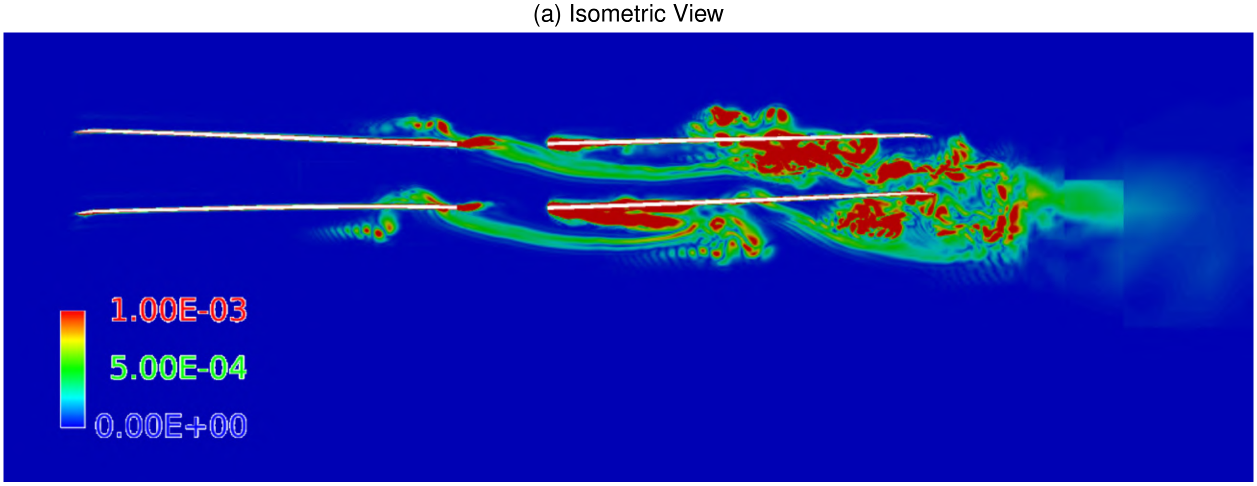

(b) Side View

Figure 42: Converged 3-D CFD flow field in isometric and side view at very high-speed flight, $\mu = 0.5$, $C_T/\sigma = 0.08$; iso-surface of Q-criterion, 0.001, colored by vorticity.

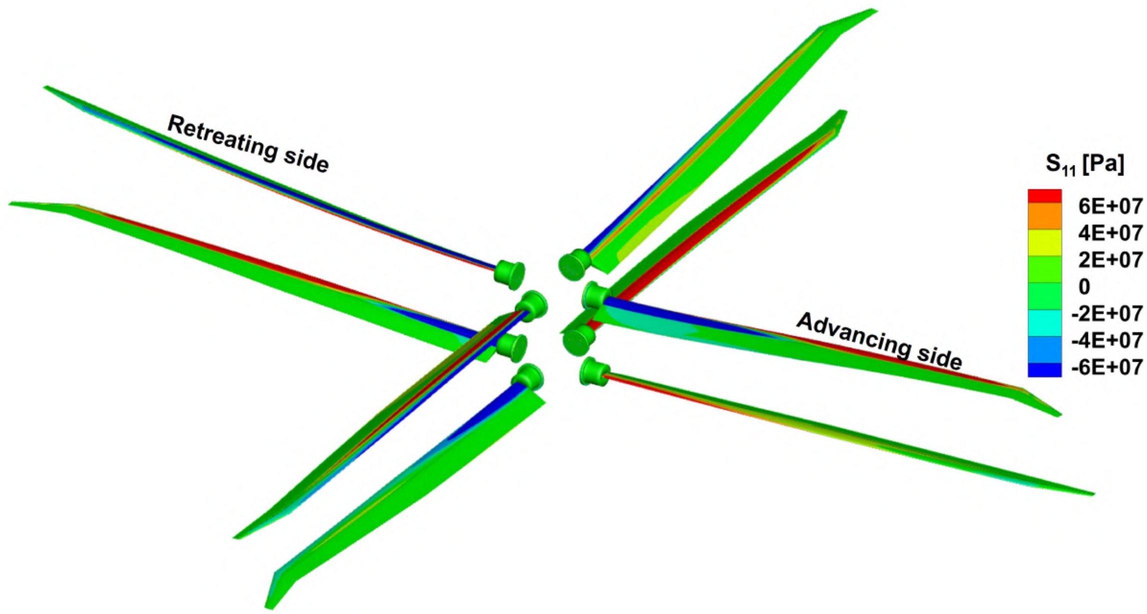

Figure 43: Axial/bending stress distribution at very high-speed flight, $\mu = 0.5$, $C_T/\sigma = 0.08$.

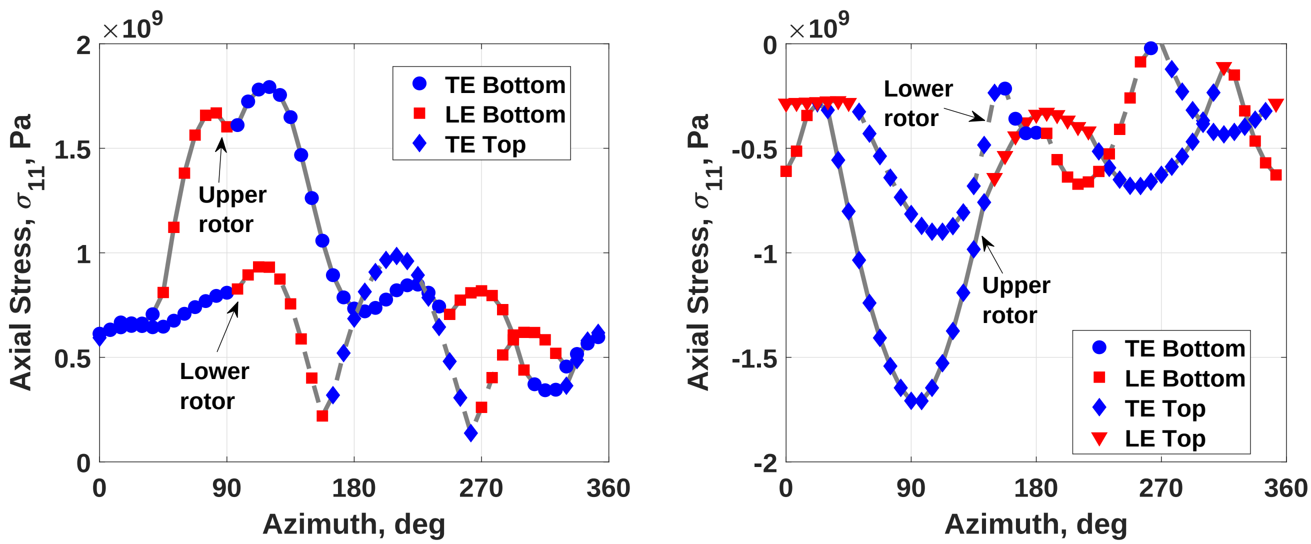

(a) Tensile stress

(b) Compression stress

Figure 44: Maximum tensile and compressive stresses versus azimuth at $\mu = 0.5$, $C_T/\sigma = 0.08$.

the trailing-edge top in the fourth quadrant. The magnitude of the stresses is $2-3$ times higher than the lower speeds ($\mu = 0.1, 0.35$), which indicates the severity of this regime. The upper rotor carries higher stresses than the lower rotor, both in tension and compression. All these observations can be visually inferred by looking at the spar deformations at different azimuths in Figures 45 and 46. These figures show the spar bending and stresses at $\psi = 0°, 90°, 180°, 270°$ for upper and lower rotors, respectively, relative to their undeformed positions. There are significant flap, lag, and torsion deformations, and these are consistent with the location of the maximum stresses.

Figure 47 shows the differential blade spar stresses over the entire rotor disk. Three things to note. First, unlike the lower speeds ($\mu = 0.1, 0.35$), the stresses do not increase or decrease in a monotonous fashion to associate with one particular bending mode; instead, the variations confirm the blade bending is contributed with the presence of flap, lag, and torsion modes. Second, unlike at high speed ($\mu = 0.35$), the upper and lower rotors show distinct patterns of stress variation across the disk. Third, the stresses are not necessarily maximum near the root at certain azimuths due to the presence of higher modes.

The shear stress patterns are even more interesting. A

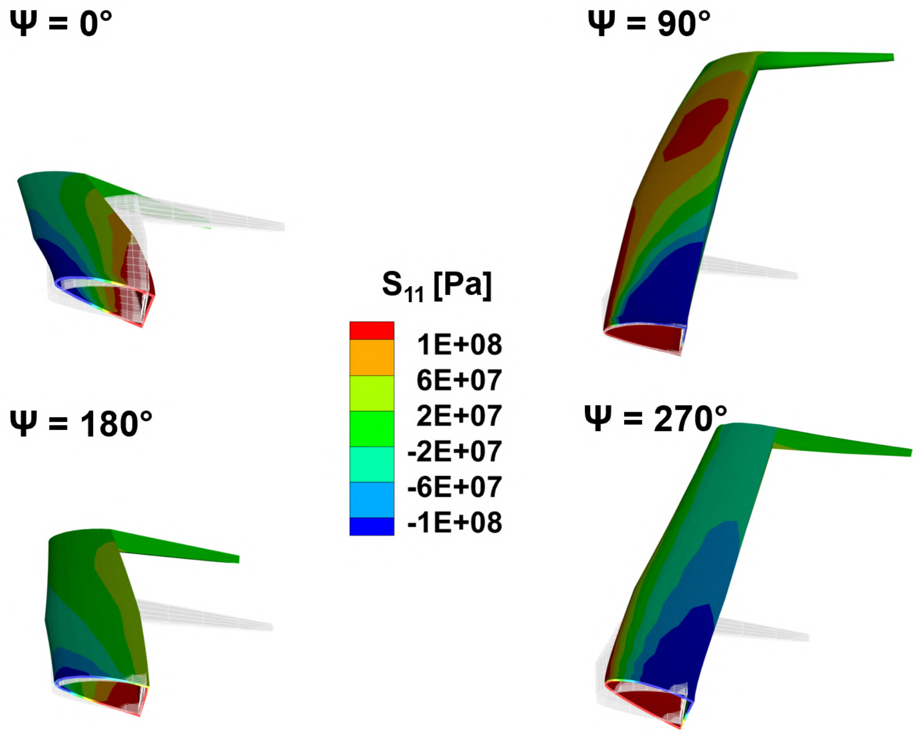

Figure 45: Upper rotor blade spar deformations and stresses at very high-speed flight, $\mu = 0.5$, $C_T/\sigma = 0.08$.

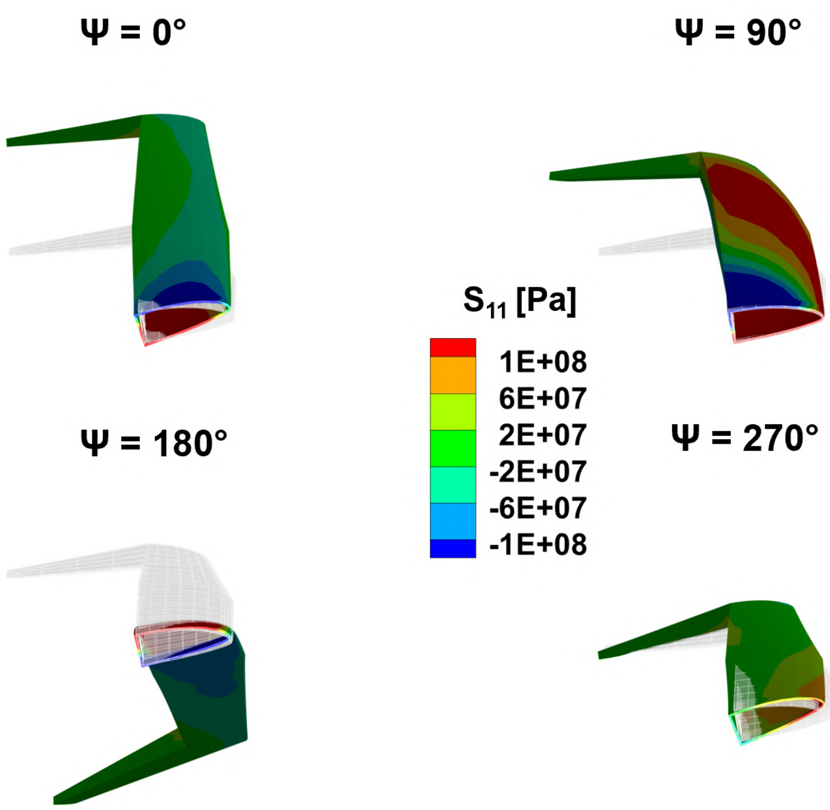

Figure 46: Lower rotor blade spar deformations and stresses at very high-speed flight, $\mu = 0.5$, $C_T/\sigma = 0.08$.

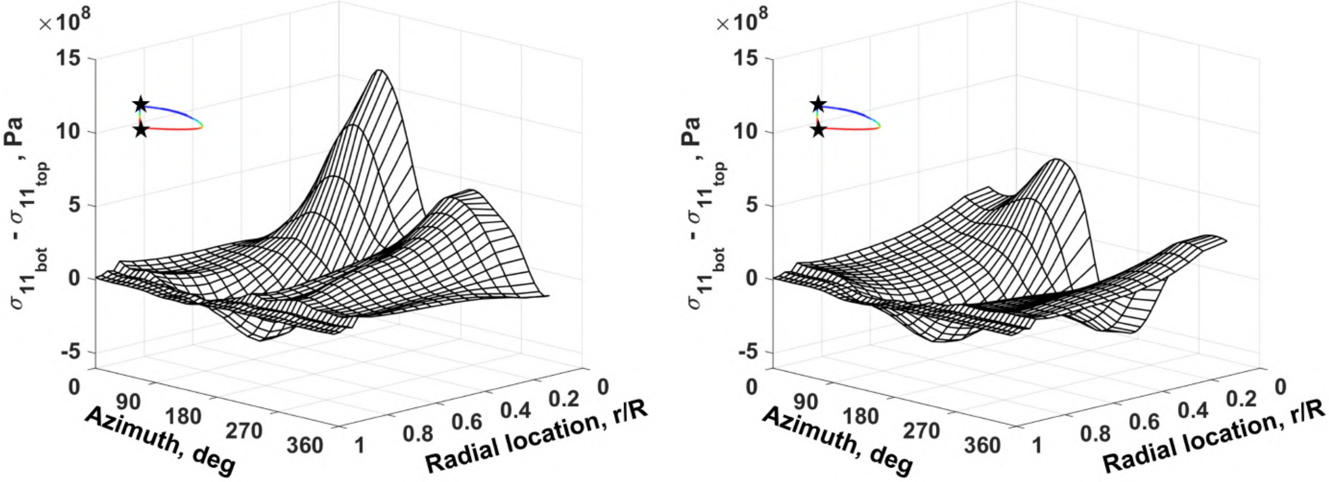

(a) Upper rotor (b) Lower rotor

Figure 47: Differential blade spar stresses (bottom - top) for upper and lower rotors at $\mu = 0.5$, $C_T/\sigma = 0.08$.

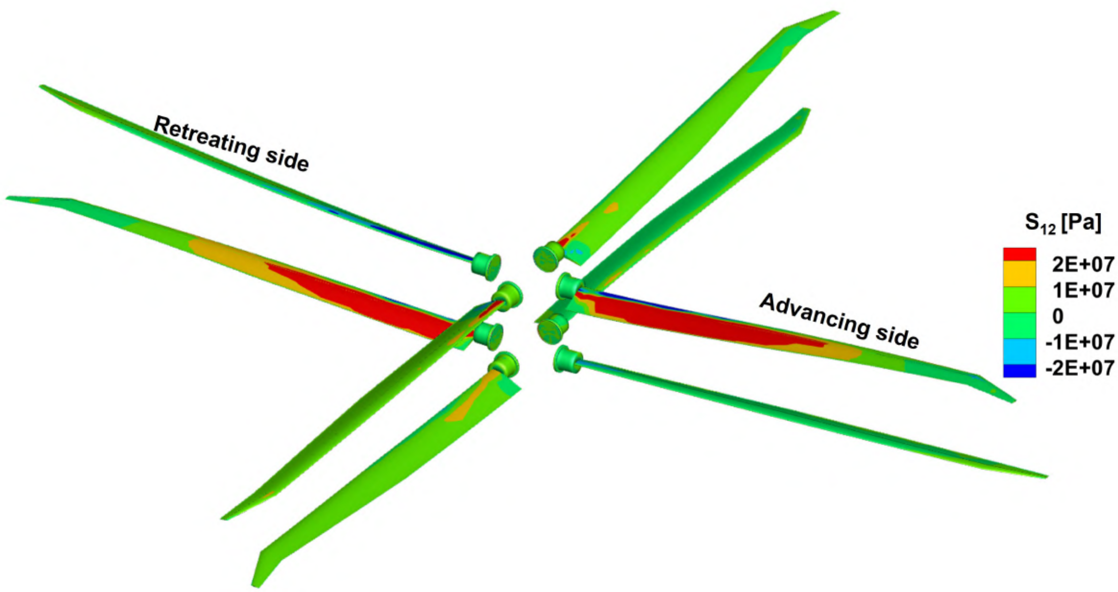

Figure 48: In-plane shear stress distribution at very high-speed flight, $\mu = 0.5$, $C_T/\sigma = 0.08$.

preliminary glimpse is given here. Figure 48 shows the in-plane shear stress σ_{12} that is nominally in-plane of the chord, whereas Figure 49 shows the transverse shear stress σ_{13} that is nominally out of plane normal to the chord. The advancing and retreating sides of the rotors carry the maximum concentrations. Even though the magnitudes are lower, they show far greater localized concentrations. The study of these and the other components, such as the inter-laminar components, remain the subject of the future.

CONCLUSIONS

This paper presented the first application of integrated 3-D analysis—defined as the coupling of 3-D finite element–based structural dynamics with 3-D RANS -based fluid dynamics—on a lift-offset coaxial rotor. The coupling was carried out with unique solvers developed to advance the current state-of-the-art. A realistic model of a modern hingeless coaxial rotor—inspired by the gross dimensions of the Sikorsky S-97 Raider—but generic and open source otherwise was developed as a showcase problem. Three level flight conditions were studied: a low-speed flight at $\mu = 0.1$ (37 knots), a high-speed flight at $\mu = 0.35$ (150 knots), and an extreme high-speed flight at $\mu = 0.5$ (220 knots). Integrated airloads and 3-D stresses were predicted and investigated. Based on this work, the following key conclusions are drawn.

1. It is possible to carry out CAD-based integrated 3-

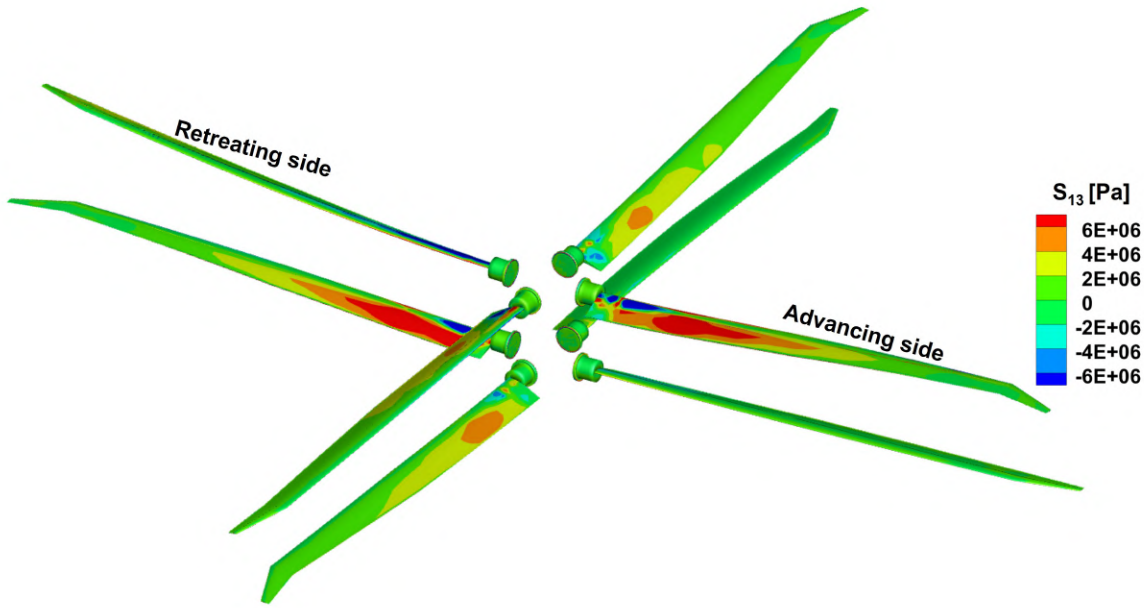

Figure 49: Transverse shear stress distribution at very high-speed flight, $\mu = 0.5$, $C_T/\sigma = 0.08$.

D aeromechanical analysis to predict aeroelastic stresses from first principles on a lift-offset coaxial rotor. The model developed here provided a practical test case for demonstration of this new methodology.

2. A tool-chain consisting of CAD, a suitable mesh generator, and scalable and parallel solvers are capable of accomplishing this task today for a coaxial rotor in about a week with about 700 processors. The 3-D structural dynamics required about 4 hours per trim iteration, so about a day of this time with 90 processors. The 3-D flow solver required 22 hours per trim iteration, so about 6 days with 568 processors. So the total time is still dominated by the flow solver.

3. The 3-D structural model development work flow is well-defined and requires no empirical inputs or lower-order cross-sectional analysis. It can be implemented at any stage of design as long as a CAD can be constructed and material properties available from the manufacturer or measured by standard coupon tests.

4. The delta-coupling methodology for rotorcraft remains valid for 3-D structures. The trick is to retain the delta of 1-D airloads to ensure convergence of the coupling while using the 3-D airloads to ensure proper structural loading. For legacy beam-based interfaces, a procedure to re-distribute the available 1-D airloads into 3-D airloads can be found.

5. At a low-speed transition flight ($\mu = 0.1$), the lower rotor carries lower steady loads but markedly higher 3-5/rev vibratory loads. This behavior was consistent with the published S-97 airload predictions from Sikorsky. The vibratory loading was observed to stem from the intertwined vortices gaining strength by ingesting the upper wake and then inducing greater impulsive loading on the lower rotor due to its proximity to those vortices.

6. At high speeds ($\mu = 0.35$ and 0.5), the inter-rotor interactions are negligible. The blade lift is dominated by the complex tip vortex roll-up from negative lift at the tip. The pitching moments and drag are dominated by the unsteady transonic shocks at the tip. The shock on the advancing blade was observed to form first on the upper surface inboard before appearing on the lower surface outboard. This was the result of extreme advancing tip Mach number and negative angles of attack from dynamic blade motions and trim controls needed for equilibrium.

7. The 8/rev blade-to-blade passage was a minor factor overall. Its effect mainly on the pitching moment suggested there is more to it than simply a bound vortex crossing. The effect was not important for structural loads. This loading is prevalent at radial stations from 50 - 80% R, and it decreases with flight speed.

8. The analysis revealed 3-D dynamic stress patterns throughout the blade but markedly on the inner half of the blade with significant concentrations further inboard of 50% R.

9. The variation of maximum stresses on the rotor disk was distinct for each flight speed. At the low speed ($\mu = 0.1$), the maximum stresses on both the upper

and lower rotors showed a dominantly 3/rev variation. This was due to the wake loading. The blade bending was predominantly in the first mode. At high speed ($\mu = 0.35$), the maximum stresses were dominantly 2/rev. This was due to the 1/rev velocity and 1/rev cyclic variations only; the torsionally stiff rotors did not produce the dramatic elastic twist observed on conventional rotors. The blade bending contained both the first and second modes. At very high speed ($\mu = 0.5$), the maximum stresses appeared to show $4-5$/rev behavior, and they also occur at different locations on the blade. The maximum stresses at this speed showed variations in all three directions—-along the span, along the chord, and along the thickness.

10. The shear stress variations were even more localized and 3-D in nature than the bending stresses.

The advent of High Performance Computing and scalable 3-D algorithms has opened the door to the world of dynamic 3-D blade and hub stresses that had remained invisible until now. The challenge now is for designers to use this insight to mitigate these stresses and for researchers to invent methods of measurements to validate them. These remain the tasks for the future.

ACKNOWLEDGEMENTS

This work was carried out at the Alfred Gessow Rotorcraft Center, University of Maryland at College Park, under the Army/Navy/NASA Vertical Lift Research Center of Excellence grant W911W61120012, with technical monitoring from Roger Strawn and Mahendra Bhagwat. We deeply appreciate their funding and support. We also wish to thank the technical points of contact: particularly William Welsh and Andreas Bernhard of Sikorsky-Lockheed Martin, Wayne Johnson of NASA, and Andrew Wissink of Army for their encouragement and guidance.

REFERENCES

1. Patil, M., and Datta, A., "A Scalable Time-Parallel Solution of Periodic Rotor Dynamics in X3D," *Journal of the American Helicopter Society*, Vol. 66, (4), October 2021, pp. 1–16. DOI: 10.4050/JAHS.66.042007

2. Wissink, A., Jude, D., Jayaraman, B., Roget, B., Lakshminarayan, V., Sitaraman, J., Bauer, A., Forsythe, J., and Trigg, R., "New Capabilities in CREATE^{TM}–AV Helios Version 11," AIAA SciTech 2021 Forum, AIAA Paper 2021-0235, January 2021. DOI: 10.2514/6.2021-0235

3. Cheney, M. C., "The ABC Helicopter," AIAA/AHS VTOL Research, Design and Operations Meeting, Atlanta, Georgia, February 17—19, 1969.

4. Blackwell, R., and Millott, T., "Dynamics Design Characteristics of the Sikorsky X2 Technology Demonstrator Aircraft," Proceedings of the American Helicopter Society 64th Annual Forum, Montreal, Quebec, Canada, May 2008.

5. Bagai, A., "Aerodynamic Design of the X2 Technology Demonstrator Main Rotor Blade," Proceedings of the American Helicopter Society 64th Annual Forum, Montreal, Quebec, Canada, May 2008.

6. Walsh, D., Weiner, S., Arifian, K., Bagai, A., Lawrence, T., and Blackwell, R., "Development Testing of the Sikorsky X2 Technology Demonstrator," Proceedings of the American Helicopter Society 65th Annual Forum, Grapevine, Texas, May 27–29, 2009.

7. Walsh, D., Weiner, S., Arifian, K., Lawrence, T., Wilson, M., Millot, T., and Blackwell, R., "High Air-speed Testing of the Sikorsky X2 Technology Demonstrator," Proceedings of the American Helicopter Society 67th Annual Forum, Virginia Beach, VA, May 3–5, 2011.

8. Lorber, P., Law, G., O'Neill, J., Matalanis, C., and Bowles, P., "Overview of S-97 RAIDER Scale Model Tests," Proceedings of the American Helicopter Society, 72nd Annual Forum, Palm Beach, Florida, May 2016.

9. Zhao, J., Xin, H., Modarres, R., and Brigley, M., "Methodology Correlation for Coaxial Rotor and Blade Load Prediction," Proceedings of the Vertical Flight Society 76th Annual Forum, October 6–8, 2020.

10. Johnson, W., *Influence of Lift Offset on Rotorcraft Performance*, NASA/TP-2009-215404, November 2009.

11. Yeo, H., and Johnson, W., "Investigation of Maximum Blade Loading Capability of Lift-Offset Rotors," *Journal of the American Helicopter Society*, Vol. 59, (1), January 2014, pp. 1–12.

12. Lim, J., McAlister, K. W., and Johnson, W., "Hover Performance Correlation for Full-Scale and Model-Scale Coaxial Rotors," *Journal of the American Helicopter Society*, Vol. 54, (3), July 2009, pp. 1–14.

13. Ramasamy, M., "Hover Performance Measurements Toward Understanding Aerodynamic Interference in Coaxial, Tandem, and Tilt Rotors," *Journal of the American Helicopter Society*, Vol. 60, (3), July 2015, pp. 1–17. DOI: 10.4050/JAHS.60.032005

14. Cameron, C., Karpatne, A., and Sirohi, J., "Performance of a Mach-Scale Coaxial Counter-Rotating Rotor in Hover," *Journal of Air-*

craft, Vol. 53, (3), March 2016, pp. 746–755. DOI: 10.2514/1.C033442

15. Uehara, D., Sirohi, J., Feil, R., and Rauleder, J., "Blade Passage Loads and Deformation of a Coaxial Rotor System in Hover," *Journal of Aircraft*, Vol. 56, (6), September 2019, pp. 2144–2157. DOI: 10.2514/1.C035469

16. Schmaus, J., and Chopra, I., "Aeromechanics of Rigid Coaxial Rotor Models for Wind-Tunnel Testing," *Journal of Aircraft*, Vol. 54, (4), July 2017, pp. 1486–1497. DOI: 10.2514/1.C034157

17. Singh, R., Kang, H., Bhagwat, M., Cameron, C., and Sirohi, J., "Computational and Experimental Study of Coaxial Rotor Steady and Vibratory Loads," AIAA SciTech 2016 Forum, AIAA Paper 2016-1787, San Diego, California, January 2016. DOI: 10.2514/6.2016-1787

18. Passe, B., Sridharan, A., Baeder, J. D., and Singh, R., "Identification of Rotor-Fuselage Aerodynamic Interactions in a Compound Coaxial Helicopter using CFD-CSD Coupling," Proceedings of the AHS Technical Conference on Aeromechanics Design for Transformative Vertical Flight, San Francisco, California, January 2016.

19. Klimchenko, V., and Baeder, J. D., "CFD/CSD Study of Interactional Aerodynamics of a Coaxial Compound Helicopter in High-Speed Forward Flight," AIAA SciTech 2020 Forum, AIAA Paper 2020-0304, Orlando, Florida, January 2020. DOI: 10.2514/6.2020-0304

20. Klimchenko, V., Sridharan, A., and Baeder, J. D., "CFD/CSD Study of the Aerodynamic Interactions of a Coaxial Rotor in High-Speed Forward Flight," AIAA Applied Aerodynamics Conference, AIAA Paper 2017-4454, Denver, Colorado, June 2017. DOI: 10.2514/6.2017-4454

21. Zhao, J., Brigley, M., and Modarres, R., "S-97 RAIDER Rotor Low Speed Vibratory Loads Analysis using CFD-CSD," AIAA SciTech 2019 Forum, AIAA Paper 2019-0860, San Diego, California, January 2019. DOI: 10.2514/6.2019-0860

22. Zhao, J., , Tuozzo, N., Brigley, M., Modarres, R., Monico, M., and Makinen, S., "CFD-CSD Support for Rotor Design Improvement to Reduce Vibrations," Proceedings of the Vertical Flight Society 77th Annual Forum, May, 2021.

23. Johnson, W., and Datta, A., "Requirements for Next Generation Comprehensive Analysis of Rotorcraft," Proceedings of the American Helicopter Society Specialist's Conference on Aeromechanics, San Francisco, CA, January 23–25, 2008.

24. Staruk, W., Datta, A., Chopra, I., and Jayaraman, B., "An Integrated Three-Dimensional Aeromechanics Analysis of the NASA Tilt Rotor Aeroacoustic Model,," *Journal of the American Helicopter Society*, Vol. 63, (3), July 2018, pp. 1–12.

25. Patil, M., and Datta, A., "Three-Dimensional Aeromechanical Analysis of Lift Offset Coaxial Rotors," AIAA SciTech 2022 Forum, AIAA Paper 2022-0928, San Diego, California, January 2022. DOI: 10.2514/6.2022-0928

26. Lumba, R., and Datta, A., "Scalable mesh partitioning for multibody-3D finite element based rotary-wing structures," *Computers and Structures*, Vol. 281, June 2023, pp. 1–21.

27. Patil, M., and Datta, A., "Three-Dimensional Blade and Hub Stresses of Coaxial Rotors in High-Speed Forward Flight," AIAA SciTech 2023 Forum, AIAA Paper 2023-1892, National Harbor, MD, January 23-27, 2023. DOI: 10.2514/6.2023-1892

28. Chi, C., Datta, A., and Panda, B., "Vacuum and Hover Tests of a Dihedral–Anhedral Tip Composite Rotor," *Journal of Aircraft*, March 2023, pp. 1–12. DOI: 10.2514/1.C037321

29. Datta, A., "X3D - A 3D Solid Finite Element Multibody Dynamic Analysis for Rotorcraft," Proceedings of the American Helicopter Society Technical Meeting on Aeromechanics Design for Vertical Lift, San Francisco, CA, January 20-22, 2016.

30. Shastry, A., and Datta, A., "Predicting Wake and Structural Loads in RPM Controlled Multirotor Aircraft," Proceedings of the Vertical Flight Society Transformative Vertical Flight Technical Meeting, San Jose, CA, January 21–23, 2020.

31. Nichols, R., and Buning, P., "OVERFLOW User's Manual, Version 2.2," NASA Langley Research Center, Hampton, VA August 2010.

32. Datta, A., Sitaraman, J., Chopra, I., and Baeder, J., "CFD/CSD Prediction of Rotor Vibratory Loads in High-Speed Flight," *Journal of Aircraft*, Vol. 43, (6), November-December 2006, pp. 1698–1709. DOI: 10.2514/1.18915

33. Potsdam, M., Yeo, H., and Johnson, W., "Rotor Airloads Prediction Using Loose Aerodynamic/Structural Coupling," *Journal of Aircraft*, Vol. 43, (3), May-June 2006, pp. 732–742. DOI: 10.2514/1.14006

34. Datta, A., Nixon, M., and Chopra, I., "Review of Rotor Loads Prediction with the Emergence of Rotorcraft CFD," *Journal of the American Helicopter Society*, Vol. 52, (4), October 2007, pp. 287–317. DOI: 10.4050/JAHS.52.287